Corrosion properties of dissimilar AA6082/AA6060 friction stir welded butt joints in different NaCl concentrations

Aleksandra Laska* (https://orcid.org/0000-0002-4872-3959)
Marek Szkodo (http://orcid.org/0000-0002-4210-0718)
Łukasz Pawłowski (https://orcid.org/0000-0002-3321-9207)
Grzegorz Gajowiec (https://orcid.org/0000-0002-9547-9813)

Faculty of Mechanical Engineering and Ship Technology, Gdansk University of Technology, Narutowicza 11/12, 80-233 Gdansk, Poland;

* Correspondence: aleksandra.laska@pg.edu.pl; Tel.: +48-698-071-526

Abstract: A solid-state friction stir welding method which is increasingly used in the marine and shipbuilding industry, has been developed to produce welds with high mechanical properties. In seawater, the oxide layer of aluminium is attacked by Cl^- ions resulting in its disruption and formation of pitting corrosion. It is particularly important to determine the electrochemical properties of the produced welds and to evaluate the effect of welding parameters on these properties. The following paper presents a study on the corrosion properties of welds of dissimilar aluminium alloys, AA6082 and AA6060, produced for two different tool traverse speeds of 160 and 200 mm/min, with consideration of the size of crystallites and residual stresses in the samples, determined by Williamson-Hall analysis and micro-indentation tests. The results revealed that the size of the crystallites in the welds was larger compared to the base materials and the friction stir welding process generated residual compressive stresses. Furthermore, the welds exhibited higher corrosion resistance compared to the parent materials. Scanning electron microscope observations indicated that the preferred locations of corrosion propagation for welds are the edges on the joint line formed by the combination of rotational and linear motion of the tool.

Keywords: friction stir welding, aluminium alloy, residual stress, Williamson-Hall analysis, corrosion, electrochemical impedance spectroscopy

1   Introduction

Aluminium and its alloys are widely used in many sectors of industry. Due to sufficient corrosion resistance and good mechanical properties, this group of materials is widely used in the maritime and shipbuilding industry [1]. Because of the susceptibility to plastic processing of aluminium and its alloys, it is possible to obtain structures with adequate mechanical strength, reducing the weight of the construction by up to three times in comparison with steel constructions [1]. This feature is extremely important for the shipbuilding industry because it allows increasing the payload of ships and reduces fuel consumption for lighter structures. In addition, the high strength-to-weight ratio of aluminium alloys contributes to the excellent manoeuvrability and stability of floating objects. 6xxx series aluminium alloys, which contain magnesium and silicon as principal alloying elements, are one of the most popular alloys used in aerospace, transportation, and marine industries [2–5].

In seawater, Cl^- ions attack oxide film protecting aluminium alloys. The breakdown of the oxide protective nano-layer results in pitting corrosion [6]. Deep pits created on the surface of aluminium components are widely observed when they are exposed to the sea water environment. Depending on the concentration of chloride anions in the solution, pitting corrosion can occur at different rates [7,8]. The average salinity of the world's marine waters is determined at 35‰ [9]. Studies conducted so far determine the corrosion properties of aluminium in such salinity [6,10–12]. However, there are water reservoirs with different salinity levels. The average salinity of the Baltic Sea is 7‰, so it is significantly lower than the world average [13,14]. There is, therefore, a supposition that the corrosion in such an environment will occur at a different rate. However, the current literature review does not allow to confirm this hypothesis.

Friction Stir Welding (FSW) is a modern method of joining materials, invented at The Welding Institute in London (TWI) and patented by Thomas et al. almost three decades ago [15]. It is a solid-state joining method that uses a specially designed non-consumable rotating tool to move along the contact line of the components to be welded. The tool consists of a pin plunged between the components and a shoulder that provides the friction between the tool and the workpiece. The contact friction generates thermal energy. The heated material is plasticised and extruded around the pin [16]. Since the melting

2

point is not reached during the process, problems associated with the changes in the volume and gas solubility are eliminated [17–19]. The FSW method allows producing butt, corner, lap, t-joints and other types of welds [20–22]. The most important process parameters include a tool geometry, a tool rotational speed, a tool traverse speed and a tilt angle [23–26]. FSW method is considered as an eco-friendly technology. Since no melting point is reached during the process, less energy is consumed compared to fusion welding techniques. Besides, the emission of CO_2 into the atmosphere can be significantly limited [27]. Controlling the process is relatively easy, and by setting optimal parameters, the necessary non-destructive testing can be subsequently minimized. Pollution generated by atomized gases for visual and magnetic inspections and radiation exposure for X-ray examinations are reduced. In addition, post-weld heat treatment is not required when optimal parameters are set [27–29]. This results in the reduction of CO_2 emissions, energy consumption and other pollutants emitted into the atmosphere.

The current literature review does not allow to determine significant correlations between particular parameters of FSW welding and electrochemical properties of the resulting welds. Qin et al. [30] studied the corrosion behaviour of the 1A14-T6 friction stir welded butt joint in the solution consisting 4 mol NaCl, 0.5 mol KNO_3 and 0.1 mol HNO_3. The joint was produced at a traverse speed of 50 mm/min, a tool rotational speed 800 rpm and a tilt angle equal to 3°. It was noticed that the joint was more resistant to exfoliation corrosion compared to the base material. In the studies of Gharavi et al. [31] AA6061-T6 FSW lap joints were tested for their electrochemical properties. The lap joint produced at the traverse speed equal to 60 mm/min, the rotational speed of 1000 rpm and the tilt angle of 3° exhibited a poorer corrosion resistance than that for the parent alloy in the solution of 3.5(wt)% NaCl. Ales et al. [32] prepared the FSW butt joints of AA2024-T4 alloy with the following process parameters: the tool traverse speed 100 mm/min, the tool rotational speed 1000 rpm, the tilt angle 2°. In the 3.5(wt)% NaCl solution it was observed that the most serious corrosion occurs in the weld nugget region.

The aim of the following study was to determine electrochemical properties of friction stir welded dissimilar AA6060/AA6082 joints and both parent alloys in seawater. The current state of the art does not allow to determine the conclusions concerning the influence of the tool traverse speed on electrochemical properties of welds of AA6082 and AA6060 aluminium alloys. The paper presents the results of tests on FSW welds produced with a different tool traverse speed.

2 Materials and methods

2.1 Friction Stir Welding

For this study AA6060 and AA6082 aluminium alloys were used. According to the producer, both alloys were solution heat-treated and artificially aged to T651 condition. The welds for the present studies were produced by the FSW method on 3 mm thick sheets. AA6082 alloy was kept on the advancing side and AA6060 on the retreating side of the welds. Chemical compositions of the chosen alloys were determined by the X-ray energy-dispersive spectrometer (EDS) (Edax Inc., Mahwah, NJ, USA) and are shown in Table 1.

Table 1. Chemical composition of AA6082 and AA6060 alloys.

Chemical composition [%wt]								
	Zn	Mg	Cr	Ti	Fe	Si	Cu	Mn	Al
AA6060	0.15	0.58	0.05	0.10	0.25	0.44	0.10	0.10	Balance
AA6082	0.20	1.03	0.25	0.10	0.50	0.90	0.10	0.42	Balance

3

The FSW welds were performed on a conventional milling machine (FU251, Friedrich Engels Kazanluk, Bulgaria). The butt welds were produced with a tool of 18 mm shoulder diameter, the distance across flats of the hexagonal pin was equal to 6 mm and the pin length was equal to 2.5 mm. The schematic illustration of the tool is shown in Figure 1 b. The shoulder plunge depth was 0.3 mm. The hexagonal pin with grooves was made of 73MoV52 (carbon 0.77%, vanadium 0.25%, molybdenum 0.65%) steel and the shoulder material was X210Cr12 (carbon 2.20%, chromium 13.00%, tungsten 0.80%) steel. The measured hardness of the pin and the shoulder were equal to 58 and 61 HRC (Wilson Mechanical Instrument Co. Inc., USA), respectively. The tilt angle (α) and the tool rotational speed (ω) were kept constant and equal to 0° and 1250 rpm, respectively, while the welds were performed at two different traverse speeds: v = 160 mm/min (W160) and 200 mm/min (W200). In accordance with the principles of the solid-state FSW method, the temperature was kept below the melting point during welding. The schematic illustration of the FSW process and the tool geometry is shown in Figure 1 a and b. Figure 1 c indicates the location of the samples cut for specific tests. Disk-shaped samples were cut from the weld nugget zone providing a sample area of 1 cm^2.
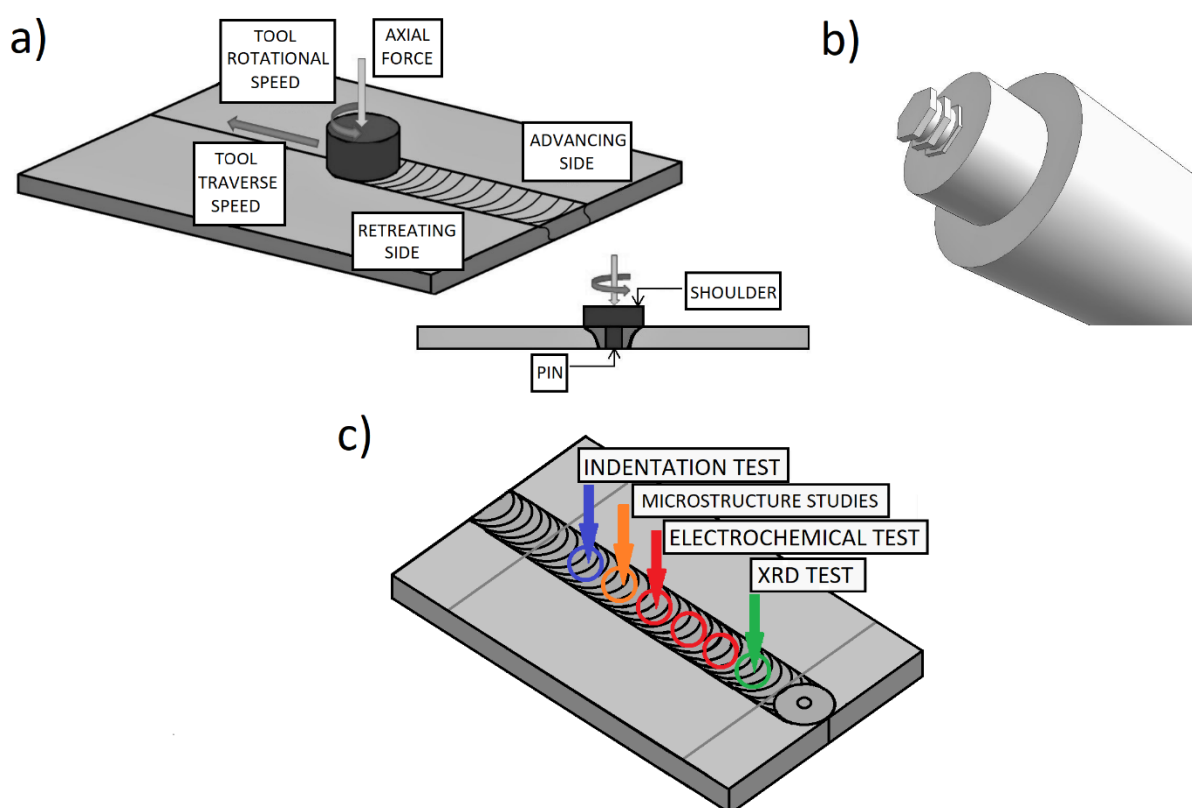
Figure 1. Schematic illustration of the FSW process (a), geometry of the tool used for FSW of AA6060/AA6082 (b) and location of the samples cut for the performed tests (c).

2.2 Material characterization

To determine the grain size of the parent materials and welds, the samples were wet ground to the final gradation #4000 and polished using a 1 µm diamond suspension. Double-stage etching in Weck's etchant was performed. Firstly, the samples were immersed in 2(wt)% NaOH solution in distilled water for 60 s. Next, the samples were etched in a reagent of 4 g KMnO$_4$, 1g NaOH and 100 ml distilled water for 10 s. The microstructure observations were performed by an optical microscope (BX51, OLYMPUS, Tokyo, Japan). For electrochemical tests, samples of the parent material and the produced welds were cut out in the shape of discs with a working surface of 1 cm^2. The samples were cleaned and degreased with isopropanol (99.7% purity, POCH, Poland).

MOST WIEDZY Downloaded from mostwiedzy.pl

The X-ray diffraction method (XRD) (Philips X'Pert Pro, Netherlands) was applied via a diffractometer (with Cu Kα radiation λ = 0.15418 nm), operated at 30 kV and 50 mA. Bragg-Brentano focusing geometry was used collecting the diffraction patterns over the 2θ range from 20° to 90° with a step size of 0.02°. A silicon standard was used to evaluate and correct instrumental broadening effects. Williamson-Hall analysis was used to estimate the size of crystallites and micro-strains in both parent materials and welds. The hardness of the samples was measured by NanoTest Vantage nanoindenter (NanoTest Vantage, Micro Materials, UK). A pyramidal Berkovich indenter was used for the tests. For each sample, 25 independent measurements were carried out with the maximum force of 10 N. The loading time was set up as 20 s, the unloading time 15 s and the dwell time at maximum force was equal to 5 s. The distance between the subsequent indents was equal to 200 μm. The load-displacement curves were recorded based on the Olivier and Pharr method. From the obtained values of reduced Young's modulus, Young's modulus was calculated by considering the following values - Poisson's ratio of diamond equal to 0.07, Poisson's ratio of aluminium 0.3 [33]. Considering calculated from Williamson-Hall analysis values of micro-strains and modulus of elasticity calculated on basis of indentation tests, the quantitative residual stresses were determined.

2.3 Electrochemical studies

Electrochemical measurements were performed using potentiostat/galvanostat (Atlas 0531, Atlas Sollich, Poland) in NaCl (99.8% purity, CHEMPUR, Poland) solutions of various concentrations: 0.2(wt)%, 0.7(wt)% and 1.2(wt)% at room temperature. The solutions were not aerated and their level of oxygen was about 24‰, according to the analysis of Shatkay [34]. The pH of all prepared solutions kept neutral (PHT-200, Voltcraft, Germany). The designation of samples with applied parameters is shown in Table 2.

Table 2. Designations of experiment samples with the applied process parameters.

Sample	Material	Welding parameters	NaCl concentration
$AA6082_{0.2}$	AA6082		0.2(wt)%
$AA6082_{0.7}$	AA6082		0.7(wt)%
$AA6082_{1.2}$	AA6082		1.2(wt)%
$AA6060_{0.2}$	AA6060	-	0.2(wt)%
$AA6060_{0.7}$	AA6060		0.7(wt)%
$AA6060_{1.2}$	AA6060		1.2(wt)%
$W160_{0.2}$	Weld AA6082/AA6060	v=160 mm/min	0.2(wt)%
$W160_{0.7}$	Weld AA6082/AA6060	ω=1250 rpm	0.7(wt)%
$W160_{1.2}$	Weld AA6082/AA6060	α=0°	1.2(wt)%
$W200_{0.2}$	Weld AA6082/AA6060	v=200 mm/min	0.2(wt)%
$W200_{0.7}$	Weld AA6082/AA6060	ω=1250 rpm	0.7(wt)%
$W200_{1.2}$	Weld AA6082/AA6060	α=0°	1.2(wt)%

A three-electrode system with a platinum electrode as counter-electrode, saturated calomel electrode as reference electrode, and aluminium samples as working electrode was used. Measurements were initiated by determining the open circuit potential (OCP) within 60 minutes. Then electrochemical impedance spectroscopy (EIS) was conducted at frequencies in the range of 1 Hz-100 kHz with a signal of 10 mV amplitude, collecting 10 points per decade. The EIS spectra were obtained at the open circuit potential value. ZView (Scribner Associates Inc., USA) software was applied to fit the obtained EIS data. The χ^2 values, representing goodness of fit, were kept on the level of 10^{-3} or lower to maintain the high reliability of the obtained results. Corrosion curves were determined using the potentiodynamic method for the potential range of -2/+1 V with a potential scan rate of 1 mV/s. Tafel extrapolation method was adopted to determine the values of the corrosive potential (E_{corr}) and the corrosion

5

current density (i_{corr}) using AtlasLab (Atlas Sollich, Poland) software. Before and after electrochemical studies the samples were weighed (Pioneer PA114CM/1, OHAUS, Greifensee, Switzerland) to determine the weight loss. The measurement results were collected at an accuracy of 0.0001 g.

2.4 Surface characterization

The surfaces of the samples before and after corrosion tests were examined using a high resolution scanning electron microscope (SEM JEOL JSM-7800 F, JEOL Ltd., Japan) with a BED detector at 5 kV acceleration voltage.

2.5 Degradation Analysis

Material degradation tests were carried out by immersion of the samples in NaCl (99.8% purity, CHEMPUR, Poland) solutions with a mass concentrations of 3.5(wt)%. The samples were kept for 168 hours at room temperature. The weight loss of the samples after this time was investigated (Pioneer PA114CM/1, OHAUS, Greifensee, Switzerland). The measurement results were collected at an accuracy of 0.0001 g. The corrosion rate (CR) based on weight loss was calculated using a formula:

$$CR\left[\frac{mm}{year}\right] = weight\ loss[g] \cdot \frac{1}{metal\ density}\left[\frac{cm3}{g}\right] \cdot \frac{1}{exposed\ area\ [cm^2]} \cdot 10\left[\frac{mm}{cm}\right] \cdot \frac{1}{exposed\ time\ [h]} \cdot 8760\left[\frac{h}{year}\right] \quad (1)$$

which can be simplified to:

$$CR\left[\frac{mm}{year}\right] = \frac{\Delta m\ [g]}{d\left[\frac{g}{cm^3}\right] \cdot S[cm^2] \cdot t[h]} \cdot 87600 \quad (2)$$

where Δm is a weight loss after the time of immersion, d is a density of the material, S is a surface area of the sample and t is the time of immersion. Densities of both aluminium alloys - AA6082 and AA6060, based on safety data sheets provided by the manufacturer, are equal to 2.710 g/cm³. To calculate the standard deviation, the test was performed 3 times.

3 Results

Figure 2 a and b shows metallographic cross-sections of W160 and W200 sample, respectively. In the cross-section of the specimen, typical FSW weld zones were distinguished – weld nugget, thermo-mechanically affected zone, heat-affected zone and base materials – AA6082 on the advancing side and AA6060 on the retreating side. In both macroscopic images of the cross-sections, the curvature of the top surface can be observed due to the tool shoulder plunge into the aluminium sheets during welding. A little material outflow, on both advancing and retreating side can be also observed. The microstructure of AA6082 and AA6060 parent materials, as well as W160 and W200 samples, is shown in Figure 2 c-f. By etching the samples, the grain size of the investigated materials could be determined. From the microscopic images it can be concluded that the weld nuggets are characterized by a more finely grained structure compared to both parent materials. Welds produced with tool traverse speeds of 160 mm/min and 200 mm/min show no significant differences in the grain size of the nugget zone. The formation of the fine-grained weld nugget (WN) is a result of the recrystallization process caused by intense plastic deformation and high heat input in this zone. The nugget experiences plastic deformations resulting from the interaction with the pin, while the frictional heating is mostly provided by the contact with the rotating shoulder. The existence of the unique zone between the base material and the heat-affected zone, called thermo-mechanically affected zone (TMAZ) is characteristic for FSW joints. Thermo-mechanically affected zone experiences both temperature and deformation, however, recrystallization cannot be observed in this zone due to insufficient deformation strain. The heat-affected zone (HAZ) is located beyond the TMAZ and experiences a thermal cycle. No plastic deformation occurs in the HAZ. The HAZ might experience a temperature rise above 250°C for a heat-

treatable aluminium alloy [35]. Although the HAZ retains the same grain structure as the parent material, the thermal exposure above 250°C causes a significant effect on the precipitate structure. The HAZ is sufficiently heated during the process so it alters the properties of that material without any plastic deformation.
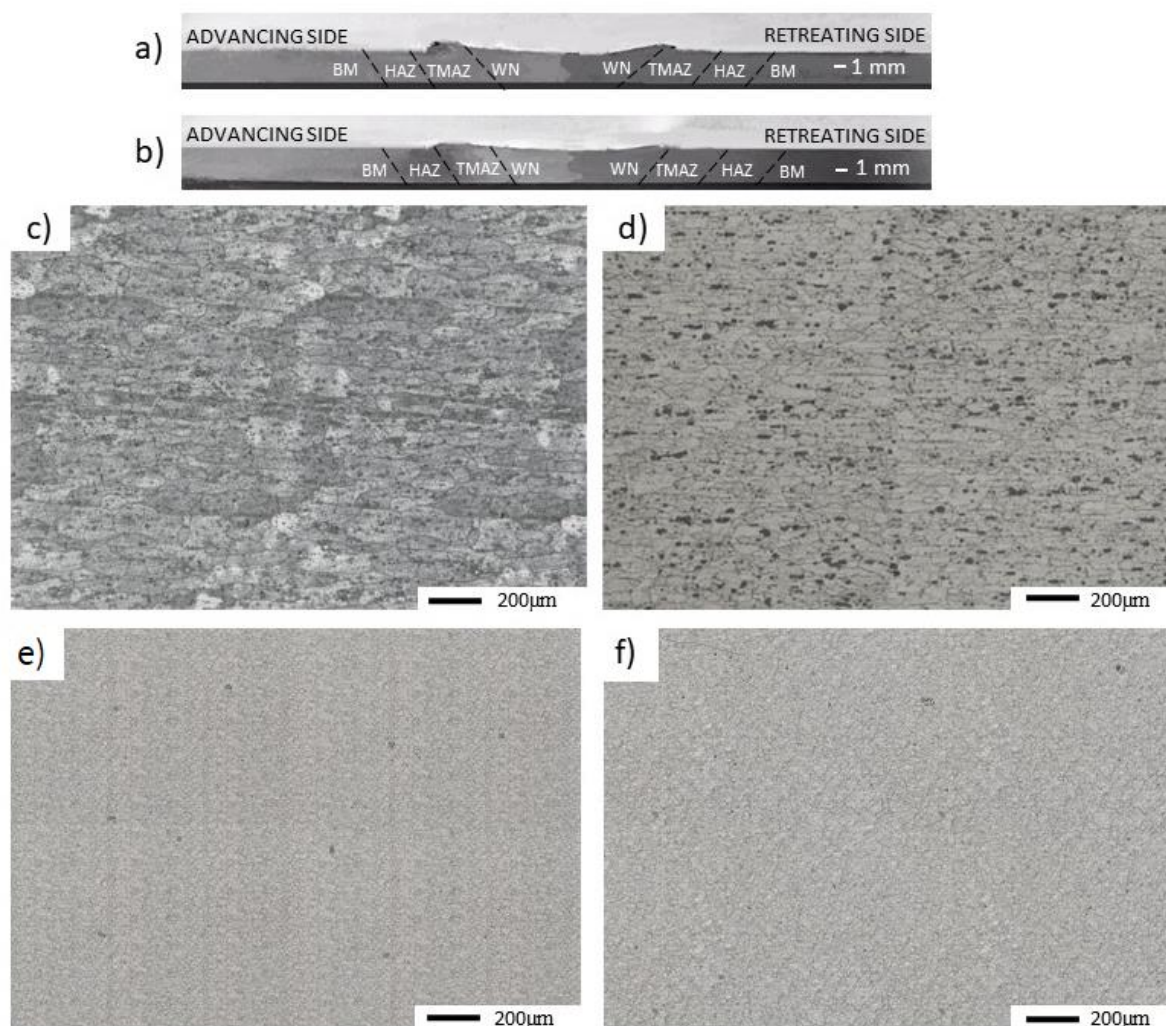
Figure 2. Metallographic cross-section of W160 (a) and W200 sample (b), optical micrographs of etched AA6082 (c) and AA6060 (d) parent materials and the weld nuggets of W160 (e) and W200 (f) samples.

Figure 3 presents X-ray diffractograms obtained for AA6082, AA6060, W160 and W200 samples. The main diffraction peaks can be indexed as originating from pure aluminium. In all the diffractograms also the peaks corresponding to phases with the main alloying elements (Mg, Mn, Si, Fe) can be observed. The diffractograms obtained for all samples also allowed the identification of aluminium oxide α-Al_2O_3 forming a passive layer on both the native materials and the welds tested. The oxide film of α-Al_2O_3 is generally reported to be present of the surface of aluminium alloys [36,37]. The crystallite size and microstrain were estimated by the Williamson-Hall analysis for the peaks assigned to aluminium. The peaks assigned to the particular phases are in agreement with the studies of Khorsand et al. [38], Leszczyńska-Madej et al. [39] and Debih et al. [40].

7
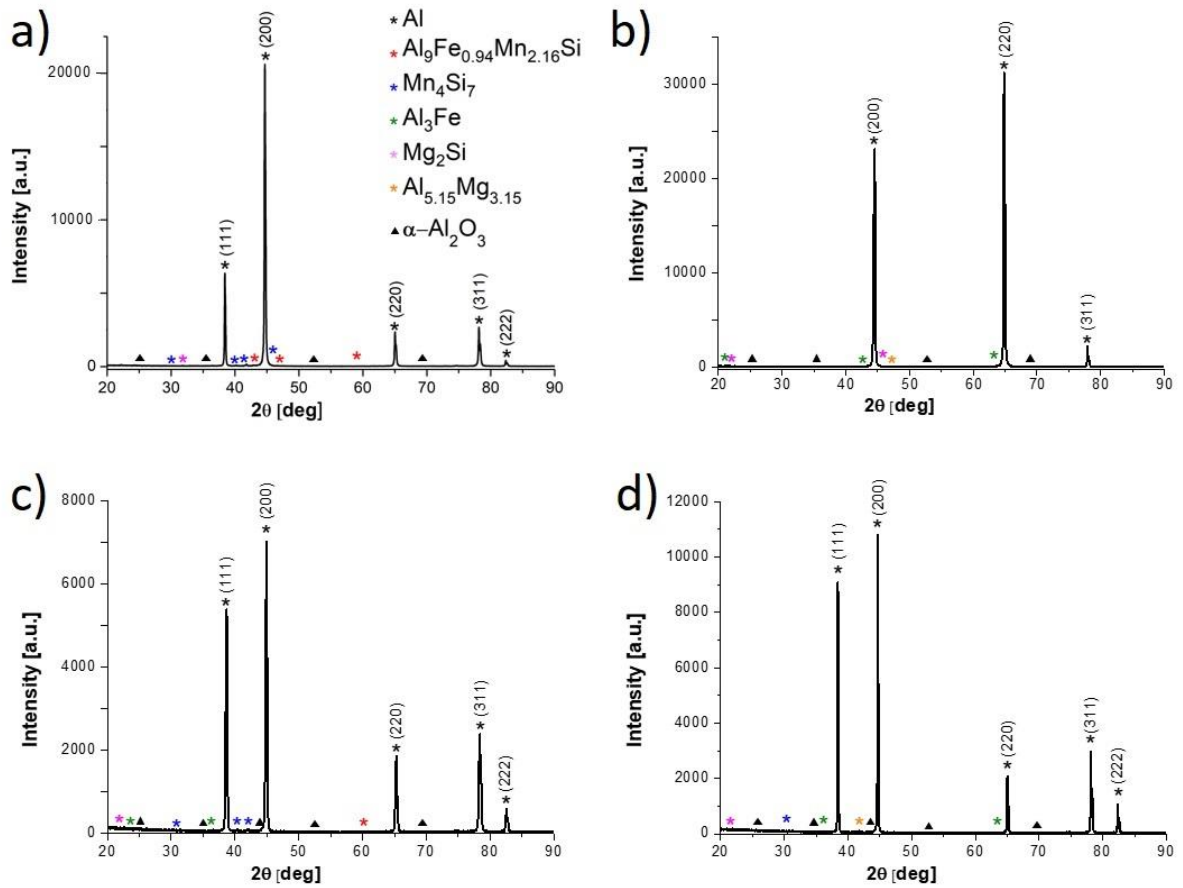
Figure 3. XRD diffraction patterns for AA6082 (a) and AA6060 (b) base materials and W160 (c) and W200 (d) welds.

The Williamson-Hall method assumes that the broadening of the peaks is due to the combination of crystallites size and microstrain [41]:

$$\beta_T = \beta_D + \beta_\varepsilon \tag{3}$$

Where β_T is the total broadening, β_D is the broadening due to the crystallite size and β_ε is the broadening resulting from strain.

From the Scherrer equation:

$$\beta_D = \frac{a_s \cdot \lambda}{L \cdot cos\theta} \tag{4}$$

Where: a_s is the Scherrer constant dependent on the shape of the crystal and the size distribution (here is assumed to be 1), λ is an electron beam wavelength (0.15418 nm) and L is a crystallite size represents a crystal portion with exactly the same crystallographic orientation such as sub-grains [42].

Similarly, the XRD peak broadening resulting to microstrain is given as:

$$\beta_\varepsilon = 4 \, \varepsilon \, tan\theta \tag{5}$$

Where ε is the strain.

Assuming equations (3), (4) and (5) the Williamson-Hall equation can be presented as:
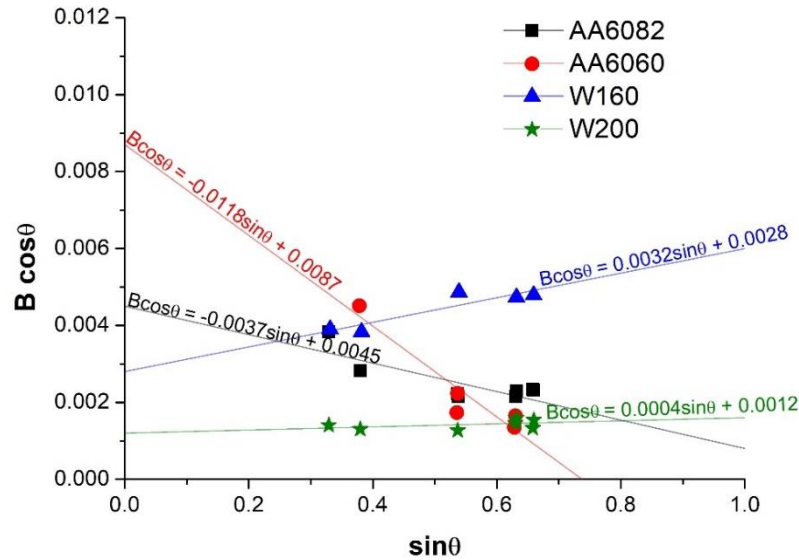
$$B = \frac{a_s \cdot \lambda}{L \cdot cos\theta} + 4 \, \varepsilon \, tan\theta \tag{6}$$

8

Or, presented as a linear function:

$$Bcos\theta = \frac{a_s \cdot \lambda}{L} + 4 \, \varepsilon \, sin\theta \qquad (7)$$

Plots of $Bcos\theta$ vs. $sin\theta$ are presented in Figure 4. Figure 4 contains the approximation of linear functions for points representing peaks in the diffraction patterns.

**Figure 4.** Plots of $Bcos\theta$ vs. $sin\theta$ for the parent materials and both welds.

The results of plot analysis, containing microstrain values and crystallite size of all the samples are shown in Table 3. The indentation tests were performed in order to calculate the reduced modulus of elasticity and the microhardness for all the tested samples. Considering the calculated Young's modulus, the values of σ_R for all the samples are also presented in Table 3. It should be noted that the residual stresses for both parent materials were below zero, which indicates the tensile nature. For both of the welds, the residual compressive stresses were observed and higher crystallite size was found. During friction stir welding a large strain of the metal matrix is observed. In combination with high temperatures during the process dynamic recrystallization occurs in the weld nugget and, consequently, a reduction in the grain size with a simultaneous increase in the size of the crystallites can be observed.

Table 3. Crystallite size, microstrain, Young modulus, residual stress and microhardness in AA6082, AA6060, W160 and W200 samples.

	L [nm]	ε [-]	E [GPa]	σ_R [MPa]	H_{ISE} [GPa]
AA6082	34.2	-0.00093	70.43 ± 4.56	-65.500 ± 4.241	1.282 ± 0.157
AA6060	17.7	-0.00295	75.22 ± 4.10	-221.899 ± 12.095	1.065 ± 0.043
W160	55.0	0.0008	74.43 ± 5.15	59.544 ± 4.120	1.519 ± 0.161
W200	128.0	0.0001	71.42 ± 4.59	7.142 ± 0.459	1.580 ± 0.171

The obtained load and unload curves for single indentation for each sample are shown in Figure 5 a. Small deflections observed on the deformation curves are caused by the temperature drift occurred with each measurement. Similar Young modulus values were observed for all the tested samples. It was evident that the welds performed higher microhardness than the parent materials. The difference in hardness between the native materials and the produced welds may be due to the difference in

9

dislocation velocities in the materials tested. The nature of the collective motion of dislocation in the crystals controls the mechanical properties, such as the microhardness of materials. The dwell time period of the indentation test was analysed to determine dislocation density and its mobility. During the indentation experiment, once the maximum load of 10 N was reached, the indenter dwelt at the maximum load for a time of 5 s. During the dwell time, the material continued to deform. The time-strain relationship during the dwell time is shown in Figure 5 b.

a)

b)
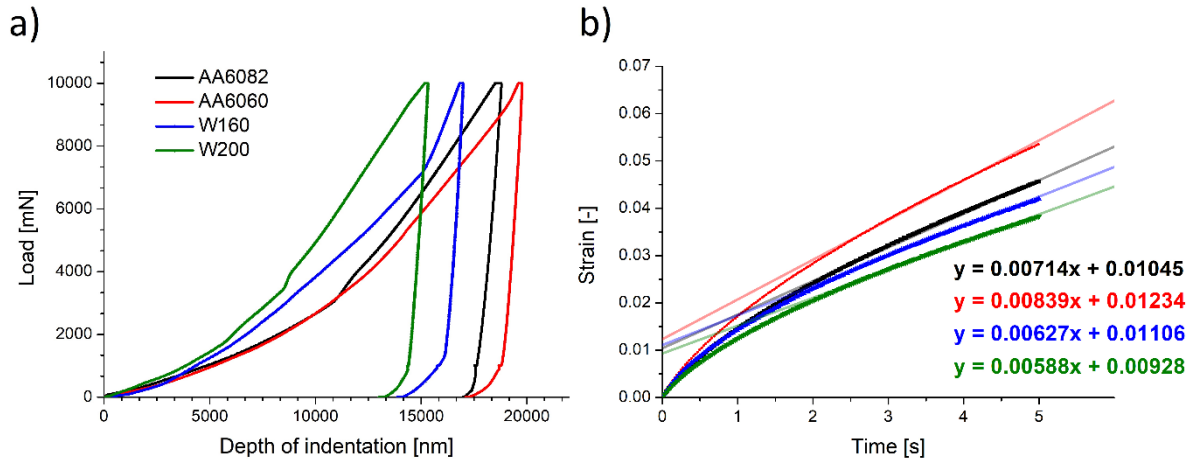
Figure 5. Hysteresis plots of load-deformation for a single indentation measurement for the analysed samples (a) and strain-time diagram for dwell period (b).

 A significant increase in the hardness of metallic materials can be observed in indentation tests at low forces. It is referred to indentation size effect (ISE). The ISE is directly related to geometrically necessary dislocations (GNDs) in the material. The density of GNDs is proportional to the inverse of the indentation depth (h). The density of GNDs is derived from the total line length k of the loop of dislocations required to form the shape of the conical indenter. These dislocations are geometrically necessary as they are introduced into the material to accommodate the indenter shape and thus provide the necessary lattice rotations. The complete line length is then divided by the hemispherical volume V defined by the contact radius a_c. The indentation depth is denoted by h, b is the Burgers vector magnitude, V is the storage volume of the GNDs, and δ is the angle between the surface and the indenter. Instead of using the volume defined by the contact radius as the storage volume of GNDs, the plastically deformed volume under the indenter is considered here. The plastic zone radius is denoted by a_{pz} and a factor f is assumed to connect a_c and a_{pz}. For most metallic materials, the plastic zone radius is larger than the contact radius, and f > 1 [43]. The geometry of the cross-section of the specimen during the indentation test is shown in Figure 6. The formula for the density of GNDs can be expressed as follows (8):

$$\rho_{GND} = \frac{3}{2} \cdot \frac{1}{f^3} \cdot \frac{tan^2\delta}{bh} \tag{8}$$
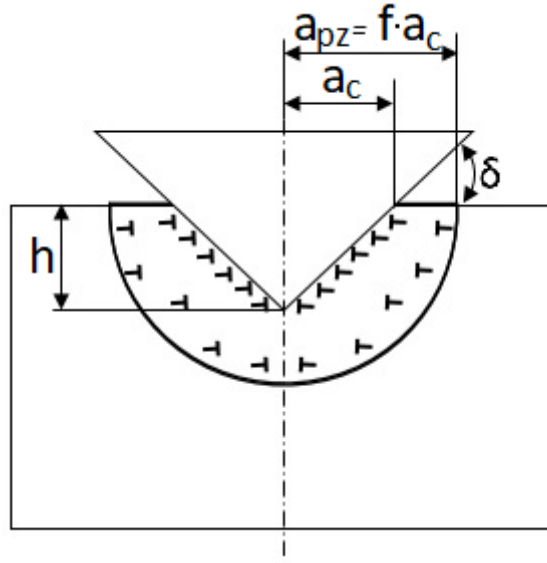
Figure 6. Geometry of the cross-section of the specimen during the indentation test.

For a cone-shaped indenter, the plasticized zone is hemispherical in shape. Although the GNDs density described above applies to the cone-shaped indenter, the same relationship between indenter displacement depth and GNDs density also exists for indenters of other shapes. For soft phases such as Al-based solid solution, the volume of the plasticized zone is much larger than the volume implied by the contact radius. For the purposes of our analysis, a factor of f = 3 can be assumed for the Berkovich indenter.

Apart from the density of GNDs and SSDs (statistically stored dislocations) the result of hardness measurement t is also affected by such factors as frictional stress of crystalline lattice H_{fr} or hardening of solid solution by dissolved alloy additives H_{ss}. The equation describing the influence of all the factors described above on the result of hardness measurement can be written as follows:

$$H_{ISE} = H_{fr} + H_{ss} + MCaGb\sqrt{\rho_{GND} + \rho_{SSD}} \tag{9}$$

where: M is the Taylor coefficient relating the shear stress to the normal stress in uniaxial deformation, C is the factor transferring the complex stress state under the indenter into a uniaxial stress state, a is a coefficient depending on the dislocation substructure, G is the transverse elastic modulus, and b is the magnitude of the Burgers vector. As a good first-order approximation, the coefficient C = 3 and the Taylor coefficient M = 3 [44]. Due to the complex stress field under the indenter, a constant value of a = 0.5 can be chosen for the dislocations GND and SSD. For Al, the Burgers vector is b = 0.286 nm and the transverse elastic modulus G = 26 GPa [45]. Dislocation hardening will only be considered in this analysis. In such a case, the relation describing the hardness including the scale effect can be written as follows:

$$H_{ISE} = MCaGb\sqrt{\rho_{GND} + \rho_{SSD}} \tag{10}$$

In contrast, the relationship between macroscopic hardness H_0 (without ISE scale effect) and dislocation density (SSD) can be described by Taylor's relation [46]:

$$H_0 = MCaGb\sqrt{\rho_{SSD}} \tag{11}$$

11

To determine the dislocation density generated during the nanoindentation tests (ρ_{GND}), use relation (8). For the Berkovich indenter, the angle δ = 24.7° and the maximum indenter displacement depths h (for plastic deformation) are registered during nanoindentation tests [47]. The H_{ISE} hardness was also determined during the nanoindentation tests. To determine the dislocation densities (ρ_{SSD}) generated during the FSW process with different parameters, the relation (10) is transformed as follows:

$$\rho_{SSD} = \frac{H_{ISE}^2}{(MC\alpha Gb)^2} - \rho_{GND} \tag{12}$$

The Orowan equation (13) was used to calculate the dislocation velocity (v) [48].

$$\frac{d\varepsilon}{dt} = \dot{\varepsilon} = b \cdot \rho_{SSD} \cdot v \tag{13}$$

In order to calculate the strain derivative as a function of time, the stabilized fragment of the creep graph of the material during the period of the maximum force during the indentation test was approximated to a linear function. The formulas of the resulting linear functions are shown in Figure 5 b. Equation 13 can be converted to the:

$$v = \frac{\dot{\varepsilon}}{b \cdot \rho_{SSD}} \tag{14}$$

The results of the above analysis are presented in Table 4.

Table 4. GNDs density, SSDs density and dislocation velocity of AA6082, AA6060, W160 and W200 samples.

	ρ_{GND} [$\frac{1}{m^2}$]	ρ_{SSD} [$\frac{1}{m^2}$]	v [$\frac{m}{s}$]
AA6082	$2.421 \cdot 10^{12}$	$1.465 \cdot 10^{15}$	$1.704 \cdot 10^{-8}$
AA6060	$2.401 \cdot 10^{12}$	$1.011 \cdot 10^{15}$	$2.903 \cdot 10^{-8}$
W160	$2.964 \cdot 10^{12}$	$2.058 \cdot 10^{15}$	$1.065 \cdot 10^{-8}$
W200	$3.161 \cdot 10^{12}$	$2.226 \cdot 10^{15}$	$0.908 \cdot 10^{-8}$

Figures 7 a, 7 c and 7 e show the variation of the open circuit potential (OCP) as a function of time obtained for the samples immersed in NaCl solution with a mass concentration of 0.2, 0.7 and 1.2%, respectively. In the case of the lowest NaCl concentration, all metallic samples reached stability in relation to the electrolyte after a few seconds of immersion in the solution. The OCP values for all the prepared samples were similar. Although lower OCP values were noted for both parent materials in comparison to the both welds, the differences were not significant. For the samples immersed in a solution of 0.7(wt)% NaCl, the stabilization of the open circuit potential was achieved after a maximum of 700 s of immersion in the electrolyte. The achieved values of OCP for all the samples were similar and they differ in the range from -0.657 V for AA6082 base material to -0.647 for AA6060 base material. The corrosion resistance studies of aluminium alloys and welds in 1.2(wt)% NaCl solution were also initiated by measuring the open circuit potential in this medium. The circuit containing AA6060 alloy and both welds achieved stability almost immediately after being placed in the electrolyte, while the circuit containing the sample of AA6082 alloy submerged in 1.2(wt)% NaCl solution achieved stability after about 2200 s after immersion. After the stability was achieved, all circuits exhibited a similar OCP value. The lowest value of -0.674 V was reported for a circuit containing a sample of AA6082 alloy and the highest OCP value for a circuit with a weld produced at a tool traverse speed of 200 mm/min and this value was equal to -0.649 V.

Based on the data from the potentiodynamic method, corrosion potential (E_{corr}) and current density (i_{corr}) of individual samples were determined on the basis of Tafel extrapolation for all NaCl concentrations. Table 5 contains the OCP, E_{corr} and i_{corr} values for the above tests.

Figures 7 b, d, f present the potentiodynamic polarization curves obtained for the samples immersed in 0.2, 0.7 and 1.2(wt)% NaCl solution, respectively. In order to obtain a corrosion curve range that allows Tafel extrapolation to be performed, a test range of -2 to 1 V potential was established. This range allows observation of both cathodic and anodic branches of the resulting polarization curve. The cathode branch of the polarization curves corresponds to the release of hydrogen, while the anode branch represents the dissolution of the substrate [49]. The E_{corr} values for both friction stir welded samples immersed in 0.2(wt)% NaCl electrolyte were higher and shifted towards positive values in comparison to AA6082 and AA60606 parent materials. The i_{corr} values for W160 and W200 samples were similar and lower in comparison to the both parent materials. It could be noted that both welds exhibited lower i_{corr} values and higher OCP values compared to both parent materials. The highest OCP values were noted for W160 and W200 samples, equal to -0.598 and -0.608 V, respectively. The highest i_{corr} values were observed for AA6082 and AA6060 alloys, 10.749 and 9.831 $\mu A \cdot cm^{-2}$, respectively. In the case of the studies of corrosion resistance in 0.7(wt)% NaCl concentration, the lowest value of i_{corr} was observed for the weld produced at a tool traverse speed of 200 mm/min. The highest i_{corr} value was reported to AA6082 base metal. It is worth noting that the particular i_{corr} values for each type of the sample were higher for 0.7(wt)% than for 0.2(wt)% NaCl concentration. Based on the potentiodynamic polarization curves values of the i_{corr} for all the samples indicate that the highest i_{corr} values were reported for the base materials, with AA6082 alloy having the value of 17.459 $\mu A \cdot cm^{-2}$. In the case of the concentration of NaCl of 1.2(wt)%, as well as for 0.2(wt)% and 0.7(wt)% NaCl concentration, the lowest value of i_{corr} was achieved with a weld produced with a tool traverse speed of 200 mm/min. The trend of higher i_{corr} values for both parent materials compared to the welds is maintained, with the weld produced at the tool traverse speed of 200 mm/min exhibiting the lowest i_{corr} value for all investigated concentrations of NaCl. These observations were in accordance with the SEM images (Figure 8), where the lowest corrosion degradation was observed for W200 samples immersed in different NaCl concentrations.
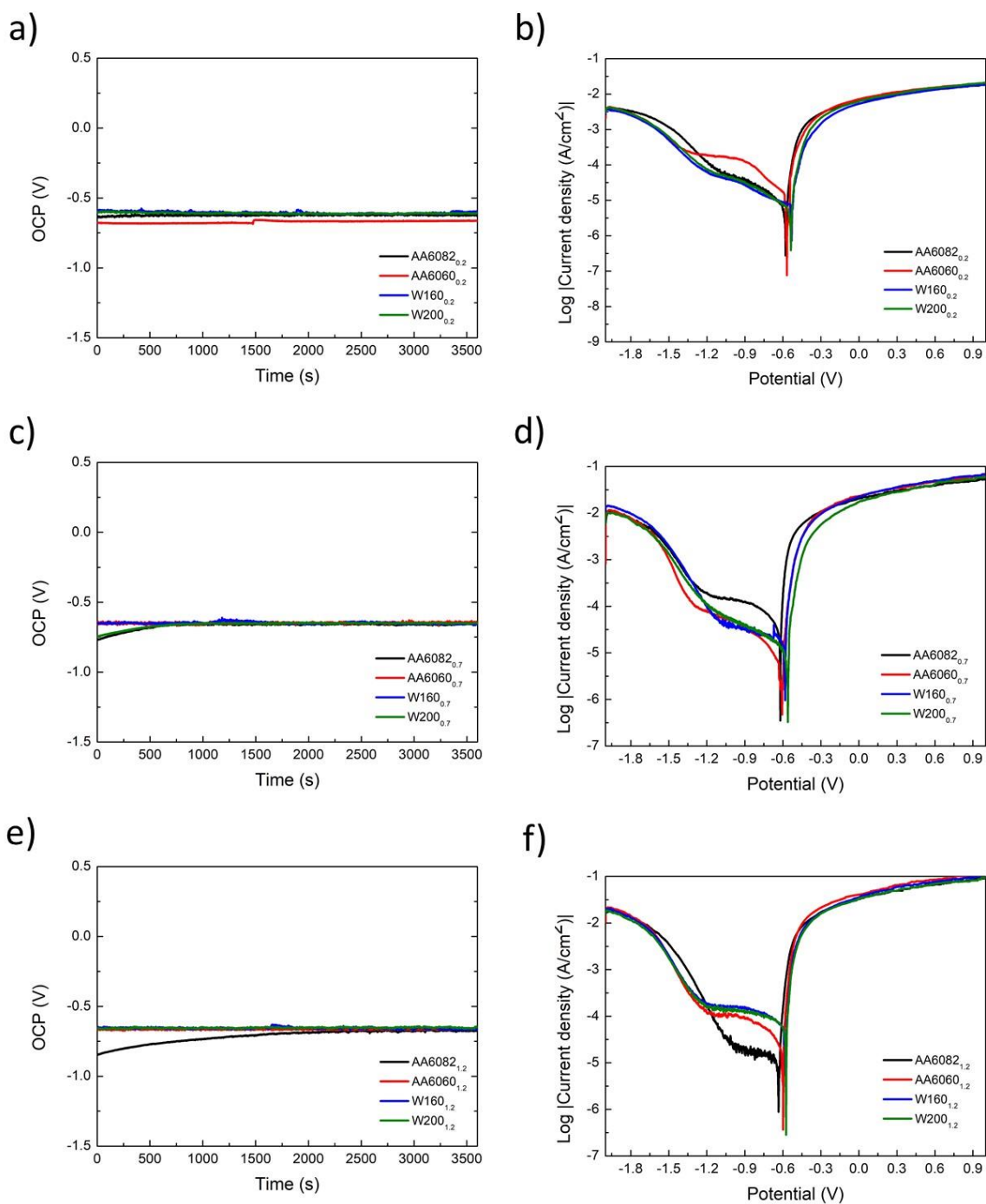
Figure 7. Open circuit potential (a, c, e) and potentiodynamic polarization curves (b, d, f) of AA6082, AA6060, W160 and W200 in NaCl solution with a concentration of 0.2(wt)% (a, b), 0.7(wt)% (c, d) and 1.2(wt)% (e, f).

Table 5. Open circuit potential (OCP), corrosion potential (E_{corr}) and current density (i_{corr}) for the prepared samples obtained after the tests in 0.2(wt)%, 0.7(wt)% and 1.2(wt)% NaCl solutions.

Sample	$AA6082_{0.2}$	$AA6060_{0.2}$	$W160_{0.2}$	$W200_{0.2}$
OCP [V]	-0.626	-0.663	-0.598	-0.608
E_{corr} [V]	-0.590	-0.557	-0.532	-0.541

14

i_{corr} [$\mu A \cdot cm^{-2}$]	10.749	9.831	8.162	8.006
Sample	**AA6082$_{0.7}$**	**AA6060$_{0.7}$**	**W160$_{0.7}$**	**W200$_{0.7}$**
OCP [V]	-0.657	-0.647	-0.653	-0.652
E$_{corr}$ [V]	-0.616	-0.611	-0.583	-0.561
i_{corr} [$\mu A \cdot cm^{-2}$]	13.381	11.107	9.983	9.426
Sample	**AA6082$_{1.2}$**	**AA6060$_{1.2}$**	**W160$_{1.2}$**	**W200$_{1.2}$**
OCP [V]	-0.674	-0.659	-0.661	-0.649
E$_{corr}$ [V]	-0.640	-0.599	-0.579	-0.576
i_{corr} [$\mu A \cdot cm^{-2}$]	17.459	16.755	15.458	13.426

The results of SEM imaging of both base materials – AA6082 on the advancing side and AA6060 on the retreating side and the welds produced with a tool traverse speed of 160 mm/min and 200 min/min are shown in Figures 8 a, 8 b, 8 c, 8 d. The base metals, mechanically and thermally unaffected during the FSW process, exhibit a similar surface appearance. In the welds produced at different tool traverse speeds, a characteristic structure relating to the rotational movement of the tool was observed. No defects of the welds were observed as a result of the welding process. Figures 8 a', 8 b', 8 c' and 8 d' show scanning electron microscope images of all samples on which electrochemical tests were performed in 0.2(wt)% NaCl solution. The effects of electrochemical corrosion were observed on all the samples. SEM images indicate that the highest corrosion degradation was observed for a sample of AA6082 parent material (a'), while the smallest losses were observed for a weld produced at a tool traverse speed of 200 mm/min (d'). Although the degradation effects for both friction stir welded samples were not significant, the material loss as a result of the corrosion process was observed in particular on edges of single strips associated with tool rotational movement. The results of observation of samples subjected to electrochemical tests at 0.7(wt)% NaCl concentration on the scanning electron microscope are presented in Figures 8 a'', 8 b'', 8 c'' and 8 d''. A significant surface porosity was observed due to numerous losses caused by galvanic corrosion. Similarly, as for the results of electrochemical tests conducted in the medium of 0.2(wt)% NaCl concentrations, in both native materials pits covered a larger surface area compared to the welds. Figures 8 a''', 8 b''', 8 c''' and 8 d''' show SEM images of the samples after electrochemical tests in 1.2(wt)% NaCl solution. The largest corrosion losses are exhibited by the AA6060 native material. Galvanic corrosion caused an increase in the porosity of the substrate and numerous losses were observed. Similar to the observations for lower NaCl concentrations, the corrosion losses for the welded samples are located mainly at the edges resulting from tool movement. This phenomenon is particularly evident in Figure 8 d'''.
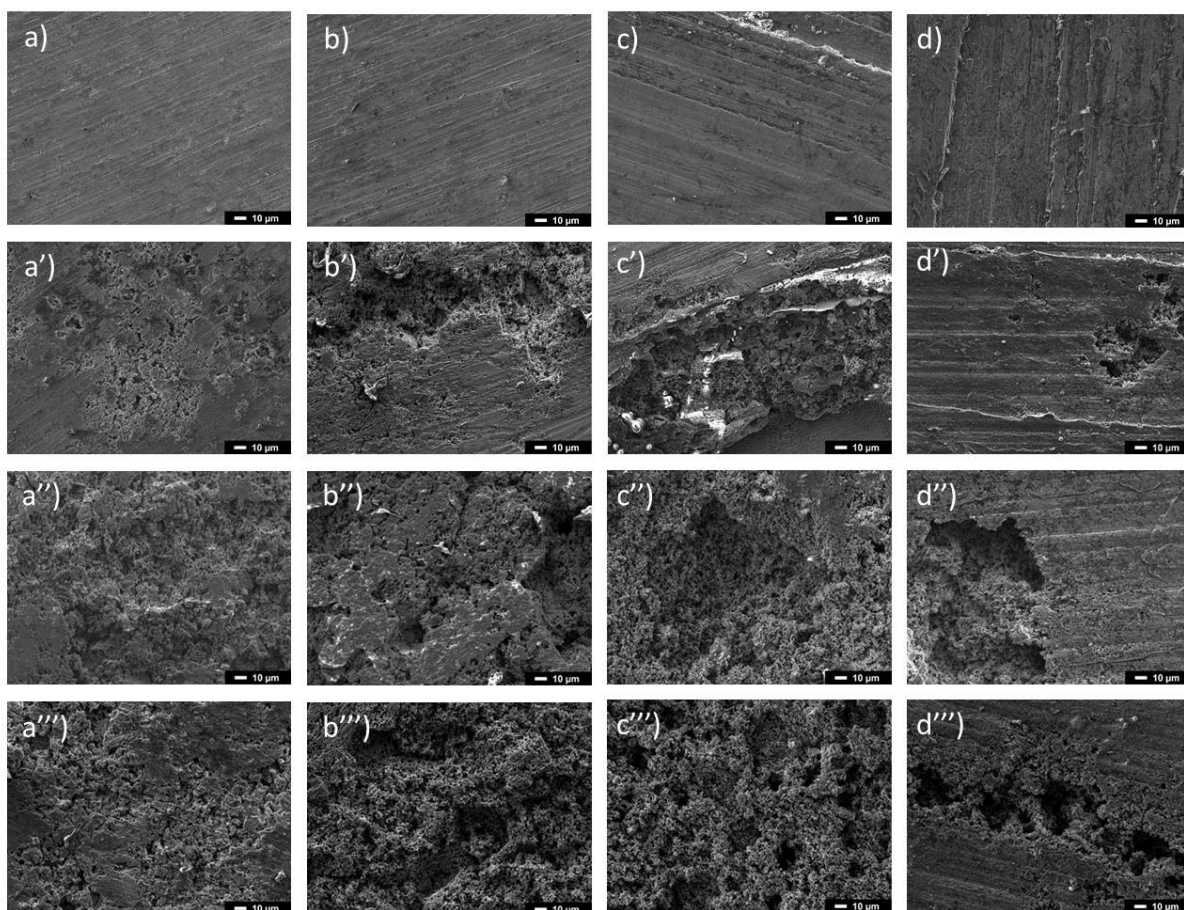
Figure 8. SEM images of the surface of AA6082 (a, a', a'', a'''), AA6060 (b, b', b'', b'''), W160 (c, c', c'', c''') and W200 (d, d', d'', d''') before electrochemical tests (a, b, c, d), after tests in electrolyte containing 0.2(wt)% NaCl (a', b', c', d'), 0.7(wt)% NaCl (a'', b'', c'', d'') and 1.2(wt)% NaCl (a''', b''', c''', d'''). Magnification x500.

The obtained EIS experimental and simulated results are presented in Figure 9. Table 6 summarizes the results of the simulations of EIS tests. Figure 9 a illustrates the proposed equivalent electrical circuit model used for fitting the obtained experimental data. It is composed of R_s representing ohmic resistance of the electrolyte, CPE_1 is a constant phase element representing the oxide layer on an aluminium alloy sample, R_2-CPE_2 loop which represents the charge transfer reaction resistance corresponding to the localised corrosion and the constant phase element of the double layer, added to the resistance of the native aluminium oxide layer (R_1). A constant phase element (CPE) was used instead of an ideal capacitor due to the roughness and unevenness of the oxide layer and the bare sample surface. The same equivalent circuit was proposed in the studies of Yu et al. [50], Kwolek et al. [51], Popa et al. [52] and de Assis et al. [53]. Figure 9 b, e, h illustrate the obtained experimental and simulated Nyquist diagrams, Figure 9 c, f, i Bode-phase angle diagrams and Figure 9 d, g, j Bode-Z diagrams.

The Nyquist diagrams obtained for the samples immersed in the electrolyte of 0.2(wt)% NaCl concentration (Figure 9 b) consisted of quarter-round capacitive loops of all examined samples. It was clearly seen that the radius of quarter-round loops of W160 and W200 samples were significantly higher than the ratios of loops representing the AA6082 and AA6060 base material samples. According to the Bode-Z diagram (Figure 9 c), the impedances of the W160 and W200 samples were higher than the impedance of both base metals throughout the whole analysed frequency range. It can be simplified that the impedance values taken by both welds were similar. The impedance values for both native materials were also similar. The Bode-phase angle (Figure 9 d) diagram allowed to note that a

16

wider maximum existed for both W160 and W200 welds in comparison to both base alloys. The radius at the medium frequency capacitive loop was higher for both welds. From the simulation results, it can be seen that R_s values for all the examined samples were roughly the same, as the electrolytes of the same chemical composition were used. The resistances of the native aluminium oxide layer were markedly higher in the case of W160 and W200 samples, comparing to both base alloys. Also, the values of charge transfer reaction resistance of W160 and W200 samples were significantly higher in comparison to base materials. CPE_1-T values, which correspond to the capacitance of the oxide layers on aluminium alloy samples were significantly lower in the case of both welded samples. The same tendency was observed in the case of CPE_2-T values, which represented the constant phase element of the double layer.

For samples immersed in the 0.7(wt)% NaCl concentration electrolytes, the obtained Nyquist diagrams, shown in Figure 9 e, consists of the capacitive loops in the shape of quarter-round. It can be noted that the radii of loops representing W160 and W200 samples were higher than the radii of loops of AA6082 and AA6060 alloys. The loop of the joint friction stir welded with a tool traverse speed of 200 mm/min was bigger than the one of the weld produced with a tool traverse speed equal to 160 mm/min. Figure 9 f shows Bode-Z graphs of all samples. At both higher and lower frequencies, the impedance value of the W160 sample was approximately the highest. The impedance values of the AA6060 sample were the lowest in almost the whole measurement frequency range. The widest maximum observed in the Bode-phase diagram (Figure 9 g) existed for the W200 sample, but the highest absolute value of phase angle around -80° was noted for the W160 sample. The EIS simulation results indicate that each sample revealed lower a R_2 value compared to the tests in 0.2(wt)% electrolyte. The base material samples exhibited similar R_2 values, more than two times lower than the both W160 and W200 samples. Also, the resistance of the native aluminium oxide layer of both friction stir welded samples were more than two times higher compared to the base materials.

Figures 9 h, i and j illustrate the obtained experimental and simulated EIS results for the samples in 1.2(wt)% NaCl environment. The loops in the Nyquist diagrams (Figure 9 h) representing W160 and W200 samples were characterized by the highest radii. Based on the Bode-Z diagram (Figure 9 i), the impedances of the W160 and W200 samples were higher in the lower frequency range, but for high frequencies, the highest impedance values were obtained for AA6082 base metal. It can be simplified that all the impedance values obtained for both welded samples were similar in all the frequency range. According to the Bode-phase diagram (Figure 9 j) the widest maxima existed for both friction stir welded samples. The obtained simulation values of the electrochemical impedance test on the samples immersed in 1.2(wt)% NaCl solution show that the resistance of the used solution differs from 9.73 to 12.66 $\Omega \cdot cm^2$ and the obtained values were notably lower than for the electrolytes of lower concentrations. The resistance of the native aluminium oxide layer was the highest for the AA6082 sample and the lowest value was obtained for the W160 sample. The values of the charge transfer resistance corresponding to the localised corrosion were the highest for the friction stir welded samples and significantly lower in the case of base metal samples. The values of the constant phase element of the double layer of AA6082, AA6060 and W160 samples were similar, but the value corresponding to W200 sample was significantly higher. It should be marked that for the W200 the value of χ^2 was the highest, which means that the results obtained were subject to the greatest uncertainty.
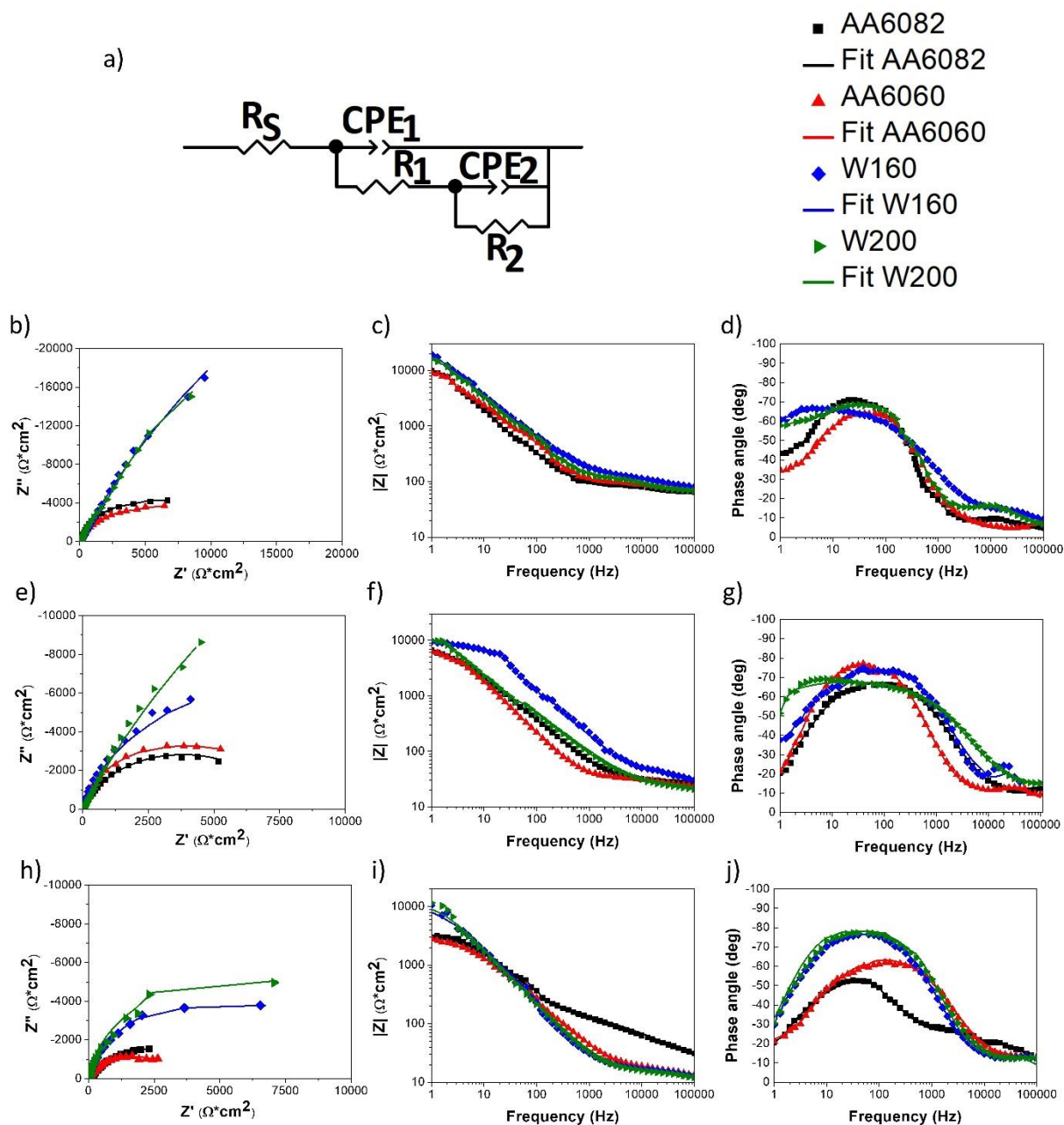
Figure 9. The equivalent circuit used to simulate experimental impedance data (a), experimental and fitted Nyquist graphs (b, e, h), Bode-Z graphs (c, f, i) and Bode-phase graphs (d, g, j) for the prepared samples in the solution with 0.2(wt)% (b, c, d), 0.7(wt)% (e, f, g), 1.2(wt)% (h, i, j) NaCl concentration.

Table 6. Simulated parameters of EIS data in 0.2(wt)%, 0.7(wt)% and 1.2(wt)% solutions of NaCl for the proposed equivalent circuit model.

	R_S [$\Omega \cdot cm^2$]	CPE$_1$-T [$\mu F \cdot cm^2$]	CPE$_1$-P	R_1 [$\Omega \cdot cm^2$]	CPE$_2$-T [$\mu F \cdot cm^2$]	CPE$_2$-P	R_2 [$\Omega \cdot cm^2$]	χ^2
AA6082$_{0.2}$	63.12	3.629	0.82	34.99	14.237	0.92	9184	0.00096164
AA6060$_{0.2}$	62.84	4.281	0.81	35.01	13.855	0.92	9333	0.00038292
W160$_{0.2}$	72.80	1.605	0.80	65.12	9.708	0.77	13677	0.0013381

18

W200$_{0.2}$	65.25	1.914	0.83	66.69	10.887	0.86	19668	0.00027963
AA6082$_{0.7}$	15.02	1.953	0.75	15.71	12.226	0.83	7577	0.00087268
AA6060$_{0.7}$	21.53	1.059	0.88	14.43	8.92	0.95	7126	0.00086053
W160$_{0.7}$	16.54	2.219	0.75	33.78	7.99	0.91	15337	0.008496
W200$_{0.7}$	21.13	1.598	0.75	34.62	4.972	0.93	17896	0.0043254
AA6082$_{1.2}$	12.66	29.754	0.55	15.77	13.728	0.81	5307	0.0015056
AA6060$_{1.2}$	9.734	19.945	0.67	10.49	13.219	0.84	3388	0.0020721
W160$_{1.2}$	10.67	2.015	0.89	7.63	13.925	0.91	9365	0.00081832
W200$_{1.2}$	11.69	4.745	0.98	10.38	21.648	0.68	11494	0.008254

To prove conclusions from the conducted electrochemical tests, the weight losses during the process for all of the samples in 0.2(wt)%, 0.7(wt)% and 1.2(wt)% NaCl concentrations were measured. The obtained results are presented in Table 7.

Table 7. Weight loss of the samples after the electrochemical tests in the solutions of 0.2%, 0.7% and 1.2% NaCl concentrations.

NaCl concentration [wt%]	0.2	0.7	1.2
	Weight loss [g/cm^2]		
AA6082	0.0029	0.0148	0.0160
AA6060	0.0026	0.0139	0.0165
W160	0.0018	0.0059	0.0085
W200	0.0009	0.0043	0.0079

Furthermore, 3.5(wt)% NaCl solution was prepared to immerse the samples of base materials and both welds and check the weight loss after 168 h. On the basis of the obtained weight losses, the corrosion rate (CR) for 3.5(wt)% concentration was calculated using formula (1). The CR values are shown in the diagram in Figure 10.
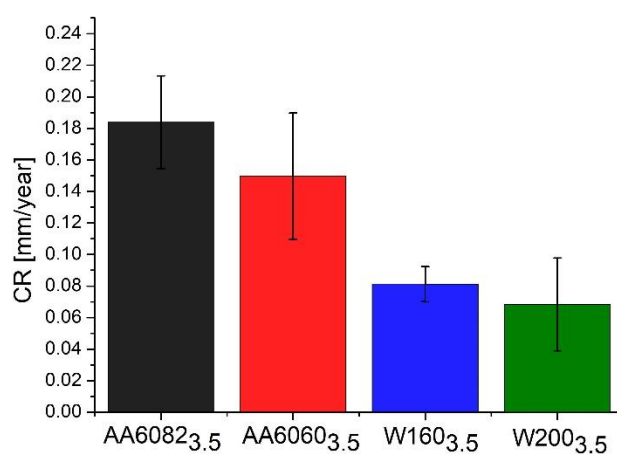
Figure 10. Corrosion rate for the samples of AA6082, AA6060, W160 and W200 immersed in 3.5(wt)% NaCl solution.

19

The data presented in the graph in Figure 10 indicate that the CR of the welds was significantly lower than that of both parent materials. It should be noted that the specific values for both welds are similar, however, the CR for the W200 weld was slightly lower. According to the Polish standard PN-78/H-04608 [54] defining a 10-grade corrosion resistance scale, both native materials represent grade 6 of the corrosion resistance in the environment of 3.5(wt)% NaCl solution. At the same time, the welds exhibit grade 5. Furthermore, according to the designations used in the standard, it can be concluded that the welds are sufficiently resistant to corrosion, while both parent materials are characterized by a limited degree of corrosion resistance. Taking into account the data in Table 7, it can be seen that the tendency of weight loss in electrochemical tests was the same for all analysed NaCl concentrations (0.2(wt)%, 0.7(wt)% and 1.2(wt)%). The weight loss of both welds was much lower than the weight loss of both parent materials for all the conducted electrochemical and degradation tests. The highest weight loss for all the tests carried out was observed for AA6082 parent material.

4   Discussion

SEM observations of the samples revealed that the native material of both alloys corroded at a faster rate than FSW welds produced at 160 and 200 mm/min. The area covered by the corrosion process was larger for AA6082 and AA6060 alloys than for W160 and W200 samples. This relationship was already observed after electrochemical tests in a solution of 0.2(wt)% NaCl. The higher corrosion resistance of FSW welds was also observed for the study of Qin et al. [30] for 2A14-T6 aluminium alloy, Zucchi et al. [55] for AA5083 alloy, and Wang et al. [56] for AA7022 alloy. Corrosion in the case of FSW welds occurred mainly on the edges of the curves resulting from the combination of rotational and linear movements of the tool. This phenomenon was evident primarily for samples corroded in the electrolyte containing 1.2(wt)% NaCl (Figure 8 d'''). It seems that this effect may result from the triaxial stress state in these places in the passive layer. Such a state of stress reduces the resistance of the passive layer to delamination during corrosive processes under the stresses. On the other hand, on flat surfaces there is a uniaxial stress state, which increases the resistance of the passive layer to its delamination. It should be noted that for lower linear speed, while maintaining the same rotational speed, there will be more such edges. Thus, a sample produced at a lower tool linear velocity may be exposed to an intensification of corrosion phenomenon due to a higher number of regions that can be considered as corrosion propagation areas. Hence, in the case of the above studies, the weld produced at a linear speed of 160 mm/min may have been more exposed to corrosion than the sample produced at a tool linear speed of 200 mm/min. Although the microscopic studies indicate higher corrosion resistance of the welds, they were unable to determine the relationship of the effect of the weld surface geometry on the corrosion resistance of the welds, and thus the tool linear speed on the electrochemical properties of the welds. SEM observations of the samples allowed qualitative determination of the corrosion losses, and subsequent quantitative analysis of the corrosion degradation rate was determined by analysing the results obtained from electrochemical tests.

Investigation of the open circuit potential of the samples immersed in 0.2(wt)% NaCl solution revealed that the welded samples had the highest OCP values. The highest OCP value of -0.598 V was observed for the sample welded with the tool traverse speed of 160 mm/min, which might indicate the highest corrosion resistance among all tested samples [57]. Also for the tests for an electrolyte with a concentration of 1.2(wt)% NaCl, the highest OCP value was observed for the welded sample, but in the case of this sample, the tool traverse speed was equal to 200 mm/min. For studies with a concentration of 0.7(wt)%, no such relationship was observed. The highest OCP value was reported for the AA6060 parent material sample, but it should be noted that the individual OCP values for all samples differed by up to 0.010 V, so the trend was not clear. The individual OCP values for all the tested samples were approximated to the E_{corr} values for these samples [58]. It could be seen that the lowest i_{corr} values

20

were noted for the friction stir welded samples produced with a tool traverse speed of 200 mm/min. However, the highest i_{corr} values were recorded for both parent materials. This relationship was evident for all NaCl concentrations. These results clearly indicate that the corrosion resistance of the welds was higher than that of the native materials, of which the weld produced with a tool traverse speed of 200 mm/min had the highest corrosion resistance. These relationships are illustrated in Figure 11 a. EIS investigations confirmed the potentiodynamic study results. The shape of the Nyquist diagrams shows that during corrosion, the process of charge transfer through the electrolyte/electrode interface is slower than mass transfer and the ongoing reaction is irreversible. The rate of this reaction is related to the rate of charge transfer. The Nyquist plots also show that the imaginary component of impedance, at the same frequency, for both FSW joint is much smaller for all concentrations of Cl$^-$ ions. This proves a much higher charge transfer resistance (R_1+R_2) and thus a lower corrosion rate of FSW joints compared to the corrosion rate of both aluminium alloys. Similarly, in the case of Bode diagrams, it can be noticed that the circuit impedance for FSW welds is higher, in almost all analysed cases, than for Al alloys. Since the circuit impedance at zero frequency is equal to the sum of the electrolyte resistance R_s and the charge transfer resistance ($R_1 + R_2$), assuming that the electrolyte resistance is the same, the resistance to charge and mass transfer through the passive layer is much greater for FSW joints. Fig. 11 b shows that the passive layer formed on FSW joints has much greater resistance to charge and mass transfer than the passive layers on aluminium alloy sheets. This suggests that the passive layer at the FSW joints has less defective structure and is more homogeneous, thus constituting a greater barrier to Al ions passing into the aqueous NaCl solution. The corrosion resistance of all tested materials decreased with increasing NaCl concentration in the solutionrelated to the increase of Cl$^-$ ions, which caused the corrosion phenomenon attacking the surface of the samples (see Fig. 11 c). However, as shown by the test results, the ranking of alloys and their joints in terms of their corrosion resistance, regardless of salinity, is as follows: W200→W160A→A6060→AA6082. Weight loss studies after a degradation test in a solution of 3.5(wt)% confirmed the previous assumptions.
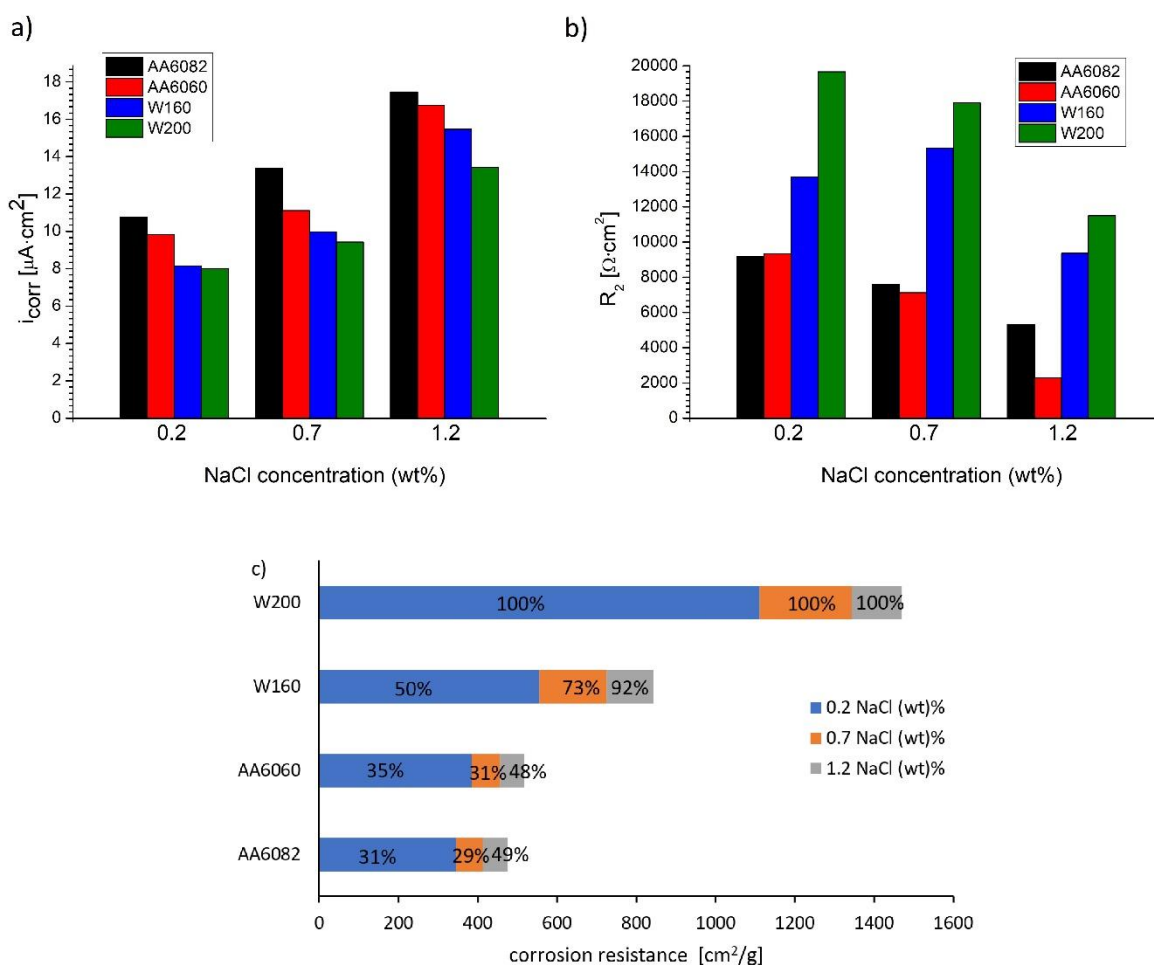
Figure 11. i$_{corr}$ (a), the charge transfer resistance (b), and corrosion resistance calculated as the mass loss reciprocal of the AA6082, AA6060, W160 and W200 samples in different NaCl concentrations (c).

The corrosion resistance of metals could be related to the crystallite size, grain size, hardness and residual stresses in the material. The results of the Williamson-Hall analysis are presented as the graphs of i$_{corr}$(L), R$_2$(L), i$_{corr}$(σ_R) and R$_2$(σ_R) in Figure 12. The obtained values were extrapolated to a linear function to determine the particular tendency.

The indentation measurements revealed that the welds performed a higher hardness than the native materials and reached 1.580 ± 0.171 and 1.519 ± 0.161 GPa for samples W200 and W160, respectively. Table 8 assumes the precipitation volume fraction identified on the XRD patterns. It should be noted that calculated values for both welded samples are lower in comparison to AA6082 parent material and higher than in case of AA6060 parent material. Indentation studies of the native materials indicated a higher hardness of the AA6082 alloy characterized by a higher volume fraction of precipitates compared to the AA6060 alloy. However, these tests also indicated higher hardness of both welds comparing to both native materials. A slightly lower hardness of 1.519 ± 0.161 GPa was observed in the W160 weld, which also had a lower precipitate content. In precipitation-strengthened alloys, such as AA6060 and AA6082, the content of precipitates has a key effect on their strength. It can be observed in the case of AA6082 and AA6060 samples that higher precipitation volume fraction resulted in higher hardness of AA6082 alloy. However, it must be noted that the welds, in comparison to both parent materials, were characterized by a more fine-grained structure due to the recrystallization process. Also, analysis in accordance with Taylor and Orowan's theories has shown

22

that welds exhibit higher dislocation densities and lower mobility of these dislocations, resulting in increased hardness in these samples.

The Williamson-Hall analysis revealed that the size of the crystallites increased due to the FSW process. In the studies of Woo et al. [59] it was reported that the AA6060-T6 weld and the native material showed no significant difference in crystallite size. In other studies of Woo et al. [60] the subgrain size before and after friction stir welding of AA6061 alloy was investigated. It was revealed that the subgrain size before the process was equal to 120 nm and after the process 130 nm. Berezina et al. [61] observed that the Williamson-Hall-Ungar analysis for the base material Al-Li-Cu-Sc-Zr alloy and FSWed sample indicated that depending on the regression profile (linear or parabolic) the calculated crystallite size is different. For the base material the value was equal to 118.9 nm, while for the weld nugget was equal to 193.18 and 70.86 nm in the case of the linear and parabolic regression, respectively. There are no extensive studies on the influence of the FSW process parameters on the crystallite size and this phenomena still needs to be explored.

As it can be seen in Figure 12 a, the crystallite growth leads to the increase of the corrosion resistance of the samples for all the investigated NaCl concentrations. In turn, the reduction in interatomic spacing due to compressive stresses on the surface can facilitate the growth and maintenance of the passivation layer. In the studies of Terasaki et al. [62] the residual stress distribution in FSW AA6063-T5 welds was investigated. The distribution of strain and residual stress in the weld is affected by the FSW welding load. The strain value is obtained by adding the positive strain value caused by the welding load to the negative strain value caused by the welding thermal cycle. Lim et al. [63] studied the residual stresses in the weld nugget of friction stir welded SUS 409 L stainless steel. It was revealed that the compressive residual stresses occurring in the nugget zone are the result of strong compression reaction by the tool shoulder. Residual tensile stresses can decrease the activation energy and surface atomic density simultaneously, thereby reducing corrosion resistance. The introduction of compressive residual stresses facilitates the formation of a passivation layer, thereby increasing corrosion resistance. The dependence of residual stress on corrosion current density (i_{corr}) and charge transfer resistance (R_2) is shown in Figure 12 b. The corrosion current density was the lowest for sample W200, which was characterized by the presence of low compressive stresses. In the case of the sample welded with a tool traverse speed of 160 mm/min, the i_{corr} values were slightly higher. The native material samples AA6082 and AA6060 exhibited much lower corrosion resistance when subjected to tensile stresses. This is evidenced by higher i_{corr} values and lower R_2 values for all analysed NaCl concentrations. These conclusions are consistent with the studies of Bai et al. [64] and Trdan et al. [65]. The relationships presented in the graphs in Figure 12 were approximated to linear functions, and Pearson correlation coefficients (IrI) for all relationships indicate moderate to high fit to linear functions [66].
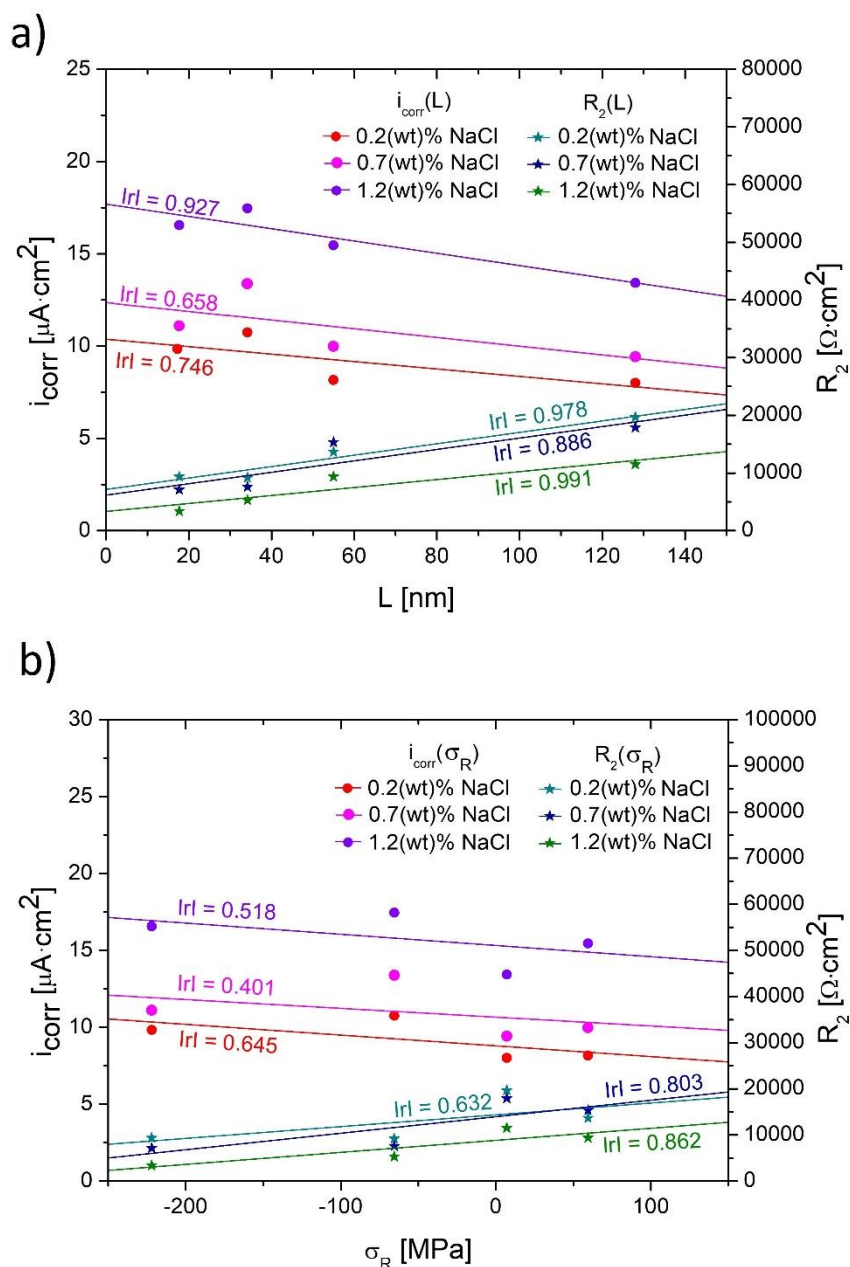
Figure 12. Relationship of corrosion current density and charge transfer resistance to crystallite size (a) and residual stress (b) in the material

However, the above relationships between i_{corr} and R_2 and the size of crystallites and residual stresses do not explain the ranking of corrosion resistance of the tested materials and FSW joints. The most corrosion-resistant W200 joint did not have the greatest residual compressive stresses and the largest crystallites. This is due to the fact that there is a mismatch in the crystal lattice between the passive layer and the substrate. The passive layer for α-Al_2O_3 is a Hexagonal Close Packed (HCP) crystal structure and lattice constant a = 0.4785 nm and c = 1.299 nm [67], and aluminium crystallizes as Face Centered Cubic structure (FCC) with a lattice constant of a = 0.4044 nm [68]. In addition, the mismatch of the crystal lattice of the passive layer and the substrate increases in the places where crystallite boundaries, grain boundaries and precipitates reinforcing the aluminium solid solution occur. It seems that the crystallite boundaries have the least influence on these disturbances, while the grain boundaries and precipitation have the greatest influence (see Fig. 13). Table 8 summarizes the type and volume fraction of the precipitates identified on the XRD patterns.
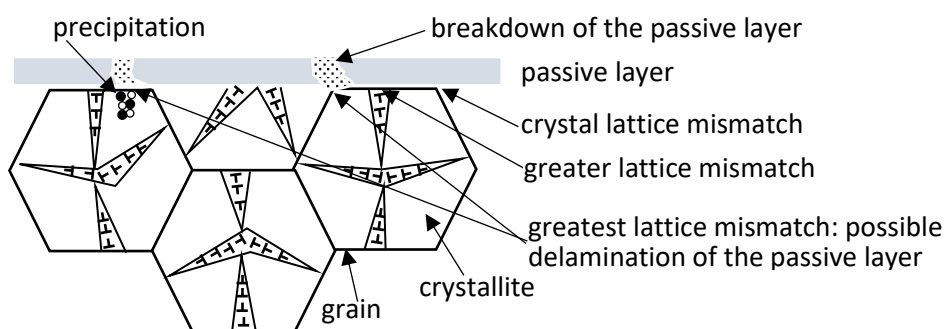
Figure 13. Schematic passive layer and substrate.

Table 8. Type and volume fraction of the precipitates identified on the XRD patterns.

	$Al_9Fe_{0.94}Mn_{2.16}Si$ %	Mn_4Si_7 %	Al_3Fe %	Mg_2Si %	$Al_{5.15}Mg_{3.15}$ %	precipitations fraction	Al. fraction
AA6082	1.146	0.700	-	0.144	-	1.99%	98.01%
AA6060	-	-	0.124	0.179	0.028	0.331%	99.669%
W160	0.104	0.365	0.335	0.241	-	1.045%	98.955%
W200	-	0.270	0.190	0.38	0.240	1.080%	98.920%

As shown in Table 8, the smallest fraction of precipitates in the structure occurs for AA6060 alloy and the highest for AA6082 alloy. Both FSW joints have a similar and average fraction of precipitates concerning both aluminum alloys. Since both the FSW joints have a greater corrosion resistance than aluminium alloys, alone fraction of the precipitates cannot affect the corrosion resistance. AA6060 and AA6082 alloys were characterized by low corrosion resistance because their manufacturing (rolling, supersaturation and artificial aging) created a structure consisting of a matrix (solid solution of alloying elements in aluminium) and coherent precipitates, which generated high tensile residual stresses. In the case of FSW joints, the structure after welding was different than for the sheets after rolling. Welding heats the material to high temperatures, which causes either partial dissolution of the precipitates in the matrix (those of smaller sizes) or loss of coherence of the precipitates with the matrix (those of larger sizes), which contributes to increasing the heterogeneity of the chemical composition of the solid solution and reducing residual tensile stresses [29]. On the other hand, welding causes a large strain of the metal matrix, which in combination with high temperature causes dynamic recrystallization and, consequently, a reduction in the grain size with a simultaneous increase in the size of the crystallites. The density of α-Al_2O_3 ranges from 3.7 to 4.15 g/cm^3 [69,70] and the density of aluminium alloys is 2.7 g/cm^3. At the same time, the modulus of elasticity of Al alloys, measured in the indentation test, is in the range of 70.43 – 75.22 GPa and for α-Al_2O_3 the stiffness is 360 GPa [71]. These differences between the physical properties of the passive layer and the substrate, as well as the low fracture toughness of the passive layer in relation to the substrate (about 5-8 MPa·m$^{1/2}$ for the passive layer and about 30 MPa·m$^{1/2}$ for the substrate [72]), mean that in the presence of tensile residual stresses, the oxide layer tends to crack, which reduces corrosion resistance, because it is easier to transfer mass and charge through cracks (see Fig. 14 a). Cracks can most easily be formed at the point contact of the oxide layer with precipitates - therefore the AA6082 alloy shows the lowest corrosion resistance, for which the volume fraction (and thus the area share, according to the Cavalieri-Hacquert principle) in the structure is about 1.99%. AA6060 alloy has slightly higher corrosion resistance due to the 6 times lower amount of precipitates compared to AA6082 alloy (despite 3 times higher tensile stresses). In turn, in the presence of compressive residual stresses, the oxide layer will tend to lose adhesion to the substrate and delamination will occur (see Fig. 14 b), especially in the place of precipitation and grain boundaries, which also lowers corrosion resistance.

25

For these reasons, the best corrosion resistance is shown by the W200 joint, for which the residual stresses are close to 0, and which has a similar number of precipitations as the W160 joint.
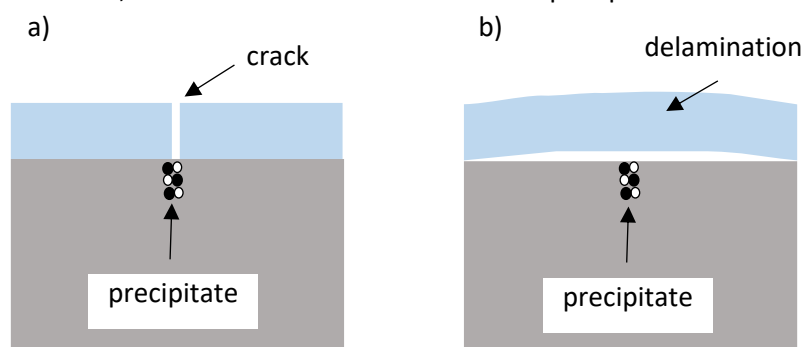

Figure 14. Schematic passive layer and substrate for tensile (a) and compressive (b) residual stress.

5   Conclusion

The above study was conducted to investigate the corrosion resistance of the welds produced by friction stir welding. Friction stir welding of dissimilar aluminium alloys AA6082 and AA6060 was performed using a tool rotational speed of 1250 rpm, a tool tilt angle of 0°, and two tool linear speeds: 160 and 200 mm/min. Williamson-Hall analysis and micro-indentation studies were performed to determine the effect of crystallite size and residual stress on corrosion resistance of the material. The obtained results allow to draw the following conclusions:

1. The crystallite size was larger in the case of the FSW welds compared to aluminum sheets.
2. Sheets manufacturing of AA6060 and AA6082 aluminium alloys generates tensile residual stresses, and welding of these sheets with the FSW method generates compressive residual stresses in the joints.
3. The linear speed 200 mm/min of welding results in lower compressive residual stresses compared to linear speed 160 mm/min.
4. The ranking of alloys and their joints in terms of their corrosion resistance, regardless of salinity, is: W200→W160A→A6060→AA6082.
5. Higher dislocation densities were observed in FSW welds, in nugget zone, compared to native materials AA6082 and AA6060. Lower dislocation velocities in the W160 and W200 samples resulted in increased hardness in the welds.
6. A linear correlation between the crystallite size and corrosion resistance, in the form of the corrosion current density, was demonstrated. The same linear correlation exists for the relationship between residual stress and corrosion resistance.
7. Degradation tests after placing the samples in 3.5(wt)% NaCl solution for 168 h confirmed the same corrosion resistance as obtained in the potentiodynamic tests and electrochemical impedance spectroscopy studies at 0.2(wt)%, 0.7(wt)% and 1.2(wt)% NaCl solution.
8. Scanning electron microscope observations indicated that the edges reflecting tool movement on the weld line can be considered as corrosion propagation centres for the welds.

Compliance with ethical standards

Conflict of interest On behalf of all authors, the corresponding author states that there is no conflict of interest.

References:

[1] Ancona A, Daurelio G, De Filippis LAC, Ludovico AD, Spera AM. CO2 Laser Welding of Aluminium Shipbuilding Industry Alloys: AA 5083, AA 5383, AA 5059, and AA 6082. XIV Int. Symp. Gas Flow, Chem. Lasers, High-Power Lasers, 2002, p. 577–87. https://doi.org/10.1117/12.515825.

[2] Dursun T, Soutis C. Recent developments in advanced aircraft aluminium alloys. Mater Des 2014;56:862–71. https://doi.org/10.1016/j.matdes.2013.12.002.

[3] Hirsch J. Aluminium in innovative light-weight car design. Mater Trans 2011;52:818–24. https://doi.org/10.2320/matertrans.L-MZ201132.

[4] Ertuğ B, Kumruoğlu C. 5083 type Al-Mg and 6082 type Al-Mg-Si alloys for ship building. Am J Eng Res 2015:146–50.

[5] Laska A, Szkodo M, Koszelow D, Cavaliere P. Effect of Processing Parameters on Strength and Corrosion Resistance of Friction Stir-Welded AA6082. Metals (Basel) 2022;12:1–16. https://doi.org/https://doi.org/10.3390/met12020192.

[6] Öteyaka MÖ, Ayrtüre H. A study on the corrosion behavior in sea water of welds aluminum alloy by shielded metal arc welding, friction stir welding and gas tungsten arc welding. Int J Electrochem Sci 2015;10:8549–57.

[7] Zeng Z, Lillard RS, Cong H. Effect of salt concentration on the corrosion behavior of carbon steel in CO2 environment. Corrosion 2016;72:805–23. https://doi.org/10.5006/1910.

[8] Han J, Carey JW, Zhang J. Effect of sodium chloride on corrosion of mild steel in CO 2-saturated brines. J Appl Electrochem 2011;41:741–9. https://doi.org/10.1007/s10800-011-0290-3.

[9] Reunamo A. Bacterial community structure and petroleum hydrocarbon degradation in the Baltic Sea. 2015.

[10] Rendón MV, Calderón JA, Fernández P. Evaluation of the corrosion behavior of the al-356 alloy in NaCl solutions. Quim Nova 2011;34:1163–6. https://doi.org/10.1590/S0100-40422011000700011.

[11] Fayomi OSI, Akande IG. Corrosion Mitigation of Aluminium in 3.65% NaCl Medium Using Hexamine. J Bio- Tribo-Corrosion 2019;5:1–7. https://doi.org/10.1007/s40735-018-0214-4.

[12] Dudzik K, Jurczak W. Influence of Friction Stir Welding on Corrosion Properties of Aw-7020M Alloy in Sea Water. Adv Mater Sci 2015;15:7–13. https://doi.org/10.1515/adms-2015-0002.

[13] Meier HEM, Kauker F. Sensitivity of the Baltic Sea salinity to the freshwater supply. Clim Res 2003;24:231–42. https://doi.org/10.3354/cr024231.

[14] Sinyavskii VS, Kalinin VD. Marine corrosion and protection of aluminum alloys according to their composition and structure. Prot Met 2005;41:317–28. https://doi.org/10.1007/s11124-005-0046-8.

[15] Thomas WM, Nicholas ED, Needham JC, Murch MG, Templesmith P, Dawes CJ. G. B. Patent Application No. 9125978.8, 1991.

[16] Sato YS, Kokawa H, Ikeda K, Enomoto M, Jogan S, Hashimoto T. Microtexture in the friction-stir weld of an aluminum alloy. Metall Mater Trans A Phys Metall Mater Sci 2001;32:941–8. https://doi.org/10.1007/s11661-001-0351-z.

[17] Kossakowski P, Wciślik W, Bakalarz M. Macrostructural Analysis of Friction Stir Welding (FSW) Joints. J Chem Inf Model 2018;01:1689–99. https://doi.org/10.1017/CBO9781107415324.004.

[18] Kah P, Rajan R, Martikainen J, Suoranta R. Investigation of weld defects in friction-stir welding and fusion welding of aluminium alloys. Int J Mech Mater Eng 2015;10. https://doi.org/10.1186/s40712-015-0053-8.

[19] Safeen MW, Spena PR. Main issues in quality of friction stir welding joints of aluminum alloy and steel sheets. Metals (Basel) 2019;9. https://doi.org/10.3390/met9050610.

[20] Zhang J, Shen Y, Yao X, Xu H, Li B. Investigation on dissimilar underwater friction stir lap welding of 6061-T6 aluminum alloy to pure copper. Mater Des 2014;64:74–80. https://doi.org/10.1016/j.matdes.2014.07.036.

[21] Rajendran C, Srinivasan K, Balasubramanian V, Balaji H, Selvaraj P. Effect of tool tilt angle on strength and microstructural characteristics of friction stir welded lap joints of AA2014-T6 aluminum alloy. Trans Nonferrous Met Soc China (English Ed 2019;29:1824–35. https://doi.org/10.1016/S1003-6326(19)65090-9.

[22] Mishra R, Ma ZY. Friction Stir Welding and Processing. Mater Sci Eng R 2005;50:1–78. https://doi.org/10.1016/j.mser.2005.07.001.

[23] Hamid HAD, Roslee AA. Study the Role of Friction Stir Welding Tilt Angle on Microstructure and Hardness. Appl Mech Mater 2015;799–800:434–8. https://doi.org/10.4028/www.scientific.net/amm.799-800.434.

[24] Colligan KJ. The friction stir welding process: An overview. Woodhead Publishing Limited; 2009. https://doi.org/10.1533/9781845697716.1.15.

[25] Machniewicz T, Nosal P, Korbel A, Hebda M. Effect of FSW Traverse Speed on Mechanical Properties of Copper Plate Joints. Materials (Basel) 2020;13:1–14. https://doi.org/doi:10.3390/ma13081937.

[26] Palanivel R, Koshy Mathews P, Murugan N, Dinaharan I. Effect of tool rotational speed and pin profile on microstructure and tensile strength of dissimilar friction stir welded AA5083-H111 and AA6351-T6 aluminum alloys. Mater Des 2012;40:7–16. https://doi.org/10.1016/j.matdes.2012.03.027.

[27] Tasi P, Hajro I, Hodži D, Dobraš D. Energy Efficient Welding Technology : Fsw. 11th Int. Conf. Accompl. Electr. Mech. Engieering Inf. Technol., 2013, p. 429–42.

[28] Sivaraj P, Kanagarajan D, Balasubramanian V. Effect of post weld heat treatment on tensile properties and microstructure characteristics of friction stir welded armour grade AA7075-T651 aluminium alloy. Def Technol 2014;10:1–8. https://doi.org/10.1016/j.dt.2014.01.004.

[29] Laska A, Szkodo M. Manufacturing Parameters, Materials, and Welds Properties of Butt Friction Stir Welded Joints–Overview. Materials (Basel) 2020;13:1–46. https://doi.org/https://doi.org/10.3390/ma13214940.

[30] Qin H long, Zhang H, Sun D tong, Zhuang Q. Corrosion behavior of the friction-stir-welded joints of 2A14-T6 aluminum alloy. Int J Miner Metall Mater 2015;22:627–38. https://doi.org/10.1007/s12613-015-1116-9.

[31] Gharavi F, Matori KA, Yunus R, Othman NK, Fadaeifard F. Corrosion evaluation of friction stir welded lap joints of AA6061-T6 aluminum alloy. Trans Nonferrous Met Soc China (English Ed 2016;26:684–96. https://doi.org/10.1016/S1003-6326(16)64159-6.

[32] Ales SK, Wang L. Effects of Friction Stir Welding on Corrosion Behaviors of AA2024-T4 Aluminum Alloy. MATEC Web Conf 2017;109:0–5. https://doi.org/10.1051/matecconf/201710902003.

[33] Frodal BH, Dæhli LEB, Børvik T, Hopperstad OS. Modelling and simulation of ductile failure in textured aluminium alloys subjected to compression-tension loading. Int J Plast 2019;118:36–69. https://doi.org/10.1016/j.ijplas.2019.01.008.

[34] Shatkay M. Dissolved oxygen in highly saline sodium chloride solutions and in the Dead Sea - measurements of its concentration and isotopic composition. Mar Chem 1991;32:89–99. https://doi.org/10.1016/0304-4203(91)90027-T.

[35] Hakem M, Khatir M, Otmani RR, Fahssi T, Debbache N, Allou D. Heat treatment and welding effects on mechanical properties and microstructure evolution of 2024 and 7075 aluminium alloys. Weld World 2007;51:163–70.

[36] Okamura H, Aota K, Sakamoto M, Ezumi M, Ikeuchi K. Behaviourof oxides during friction stir welding of aluminium alloy and their effect on its mechanical properties. Weld Int 2002;16:266–75. https://doi.org/10.1080/09507110209549530.

[37] Zeng XH, Xue P, Wang D, Ni DR, Xiao BL, Wang KS, et al. Material flow and void defect formation in friction stir welding of aluminium alloys. Sci Technol Weld Join 2018;23:677–86. https://doi.org/10.1080/13621718.2018.1471844.

[38] Khorsand S, Huang Y. Integrated Casting-Extrusion (ICE) of an AA6082 Aluminium Alloy. Miner Met Mater Soc 2017:1357–64. https://doi.org/DOI 10.1007/978-3-319-51541-0_32.

[39] Leszczyńska-Madej B, Richert M, Wąsik A, Szafron A. Analysis of the microstructure and selected properties of the aluminium alloys used in automotive air-conditioning systems. Metals (Basel) 2018;8. https://doi.org/10.3390/met8010010.

[40] Debih A, Ouakdi EH. Anisotropic thermomechanical behavior of AA6082 aluminum alloy Al-Mg-Si-Mn. Int J Mater Res 2018;109:34–41. https://doi.org/10.3139/146.111580.

[41] Williamson GK, Hall WH. X-ray line broadening from filed aluminium and wolfram. Acta Metall 1953;1:22–31. https://doi.org/10.1016/0001-6160(53)90006-6.

[42] Khoshkhoo MS, Scudino S, Thomas J, Surreddi KB, Eckert J. Grain and crystallite size evaluation of cryomilled pure copper. J Alloys Compd 2011;509:S343–7. https://doi.org/10.1016/j.jallcom.2011.02.066.

[43] Durst K, Backes B, Franke O, Göken M. Indentation size effect in metallic materials: Modeling strength from pop-in to macroscopic hardness using geometrically necessary dislocations. Acta Mater 2006;54:2547–55. https://doi.org/10.1016/j.actamat.2006.01.036.

[44] Johnson KL. Contact Mechanics. Cambridge University Press; 1985. https://doi.org/10.1017/CBO9781139171731.

[45] Cho J, Molinari JF, Anciaux G. Mobility law of dislocations with several character angles and temperatures in FCC aluminum. Int J Plast 2017;90:66–75. https://doi.org/10.1016/j.ijplas.2016.12.004.

[46] Zhuang Z, Liu Z, Cui Y. Strain Gradient Plasticity Theory at the Microscale. Dislocation Mech. Cryst. Plast., 2019, p. 57–90. https://doi.org/10.1016/b978-0-12-814591-3.00003-0.

[47] Yamada H, Ogasawara N, Shimizu Y, Horikawa H, Kobayashi H. Effect of high strain rate on micro-indentation test in pure aluminum. EPJ Web Conf 2012;26:2–6. https://doi.org/10.1051/epjconf/20122601028.

[48] Voyiadjis GZ, Abed FH. Effect of dislocation density evolution on the thermomechanical response of metals with different crystal structures at low and high strain rates and temperatures. Arch Mech 2005;57:299–343. https://doi.org/10.24423/aom.190.

[49] Cassayre L, Chamelot P, Arurault L, Taxil P. Anodic dissolution of metals in oxide-free cryolite melts. J Appl Electrochem 2005;35:999–1004. https://doi.org/10.1007/s10800-005-6727-9.

[50] Yu M, Zhao X, Xiong L, Xue B, Kong X, Liu J, et al. Improvement of corrosion protection of coating system via inhibitor response order. Coatings 2018;8:1–15. https://doi.org/10.3390/coatings8100365.

[51] Kwolek P. Corrosion behaviour of 7075 aluminium alloy in acidic solution. RSC Adv 2020;10:26078–89. https://doi.org/10.1039/d0ra04215c.

[52] Popa M V., Vasilescu E, Drob P, Vasilescu C, Drob SI, Mareci D, et al. Corrosion resistance improvement of titanium base alloys. Quim Nova 2010;33:1892–6. https://doi.org/10.1590/S0100-40422010000900014.

[53] de Assis SL, Costa I. The effect of polarisation on the electrochemical behavior of Ti-13Nb-13Zr alloy. Mater Res 2007;10:293–6. https://doi.org/10.1590/s1516-14392007000300014.

[54] PN-H-04608:1978 Korozja metali -- Skala odporności metali na korozję. 1978.

[55] Zucchi F, Trabanelli G, Grassi V. Pitting and stress corrosion cracking resistance of friction stir welded AA 5083. Werkstoffe Und Korrosion 2001;52:853–9. https://doi.org/10.1002/1521-4176(200111)52:11<853::aid-maco853>3.0.co;2-1.

[56] Wang HF, Wang JL, Song WW, Zuo DW, Shao DL. Analysis on the corrosion performance of friction stir welding joint of 7022 aluminum alloy. Int J Electrochem Sci 2016;11:6933–42. https://doi.org/10.20964/2016.08.09.

[57] Łosiewicz B, Maszybrocka J, Kubisztal J, Skrabalak G, Stwora A. Corrosion resistance of the cpti g2 cellular lattice with tpms architecture for gas diffusion electrodes. Materials (Basel) 2021;14:1–18. https://doi.org/10.3390/ma14010081.

[58] Berradja A. Electrochemical Techniques for Corrosion and Tribocorrosion Monitoring: Methods for the Assessment of Corrosion Rates. Corros. Inhib., 2019, p. 1–26. https://doi.org/10.5772/intechopen.86743.

[59] Woo W, Ungár T, Feng Z, Kenik E, Clausen B. X-ray and neutron diffraction measurements of dislocation density and subgrain size in a friction-stir-welded aluminum alloy. Metall Mater Trans A Phys Metall Mater Sci 2010;41:1210–6. https://doi.org/10.1007/s11661-009-9963-5.

[60] Woo W, Feng Z, Hubbard CR, David SA, Wang XL, Clausen B, et al. In-situ time-resolved neutron diffraction measurements of microstructure variations during friction stir welding in a 6061-T6 aluminum alloy. ASM Proc Int Conf Trends Weld Res 2009:407–12. https://doi.org/10.1361/cp2008twr407.

[61] Berezina A, Molebnyi O. Structural changes in friction-stir welded Al-Li-Cu-Sc-Zr (1460) alloy. Nanomater Appl Prop 2016;2.

[62] Terasaki T, Akiyama T. Mechanical Behavior of Joints in FSW: Residual Stress , Inherent Strain and Heat Input Generated by Friction Stir Welding. Weld World 2003;47:24–31.

[63] Lim Y-S, Kim S-H, Lee K-J. Effect of residual stress on the mechanical properties of fsw joints with SUS409L. Adv Mater Sci Eng 2018:1–8.

[64] Bai LY, Gao L, Jiang KB. Influence of Residual Stress on the Corrosion Behaviors of Welded Structures in the Nature Seawater. IOP Conf Ser Mater Sci Eng 2018;392. https://doi.org/10.1088/1757-899X/392/4/042009.

[65] Trdan U, Grum J. Investigation of corrosion behaviour of aluminium alloy subjected to laser

shock peening without a protective coating. Adv Mater Sci Eng 2015;2015.
https://doi.org/10.1155/2015/705306.

[66]   Saccenti E, Hendriks MHWB, Smilde AK. Corruption of the Pearson correlation coefficient by
measurement error and its estimation, bias, and correction under different error models. Sci
Rep 2020;10:1–20. https://doi.org/10.1038/s41598-019-57247-4.

[67]   Chen DY, Shao MW, Cheng L, Wang XH, Ma DDD. Strong and stable blue photoluminescence:
The peapodlike SiO_x @ Al_2O_3 heterostructure. Appl Phys Lett 2009;94:2007–10.
https://doi.org/10.1063/1.3070319.

[68]   Morinaga M. A Quantum Approach to Alloy Design. 2019. https://doi.org/10.1016/b978-0-12-
814706-1.00013-3.

[69]   Munro RG. Evaluated material properties for a sintered α-alumina. J Am Ceram Soc
1997;80:1919–28. https://doi.org/10.1111/j.1151-2916.1997.tb03074.x.

[70]   Kimura T, Matsuda Y, Oda M, Yamaguchi T. Effects of agglomerates on the sintering of alpha-
Al_2O_3. Ceram Int 1987;13:27–34. https://doi.org/10.1016/0272-8842(87)90035-6.

[71]   De Faoite D, Browne DJ, Chang-Díaz FR, Stanton KT. A review of the processing, composition,
and temperature-dependent mechanical and thermal properties of dielectric technical
ceramics. J Mater Sci 2012;47:4211–35. https://doi.org/10.1007/s10853-011-6140-1.

[72]   Szkodo M, Stanisławska A, Komarov A, Bolewski Ł. Effect of MAO coatings on cavitation
erosion and tribological properties of 5056 and 7075 aluminum alloys. Wear 2021;474–475.
https://doi.org/10.1016/j.wear.2021.203709.

Aleksandra Laska She is a PhD student in the discipline of Mechanical
Engineering at Gdańsk University of Technology, Faculty of
Mechanical Engineering and Ship Technology, Institute of Machines
and Materials Engineering. Her research topics focus on Friction Stir
Welding method, with particular emphasis on the investigations of
residual stresses in the joints. Her research area includes aluminium
and its alloys in engineering applications.

Marek Szkodo He works in two scientific disciplines: Materials Engineering and Mechanical Engineering. He is the author of many publications on the environmental degradation of engineering materials and the use of Friction Stir Welding Method in engineering applications. He is a graduate of the Faculty of Mechanical Engineering at the Gdańsk University of Technology.

Łukasz Pawłowski Research assistant and PhD student at the Institute of Machines and Materials Technology, Faculty of Mechanical Engineering and Ship Technology, Gdansk University of Technology. His research work concerns surface modification and characterization of titanium and titanium alloys. His research area includes electrochemical studies on metals and polymers.

Grzegorz Gajowiec He is a graduate of the faculty of Mechanical Engineering at the Gdańsk University of Technology. He is the author of many expert opinions for the industry. He deals with environmental degradation of engineering materials and scanning electron microscopy.